

# LoCuSS: First Results from Strong-lensing Analysis of 20 Massive Galaxy Clusters at $z=0.2$

Johan Richard,<sup>1\*</sup> Graham P. Smith,<sup>2</sup> Jean-Paul Kneib,<sup>3</sup> Richard S. Ellis,<sup>4</sup>  
A. J. R. Sanderson,<sup>2</sup> L. Pei,<sup>4</sup> T. A. Targett,<sup>5</sup> D. J. Sand,<sup>6,7</sup> A. M. Swinbank,<sup>1</sup>  
H. Dannerbauer,<sup>8</sup> P. Mazzotta,<sup>9</sup> M. Limousin,<sup>3,10</sup> E. Egami,<sup>11</sup> E. Jullo,<sup>12</sup>  
V. Hamilton-Morris,<sup>2</sup> S. M. Moran,<sup>13</sup>

<sup>1</sup> *Institute for Computational Cosmology, Department of Physics, Durham University, South Road, Durham, DH1 3LE, England*

<sup>2</sup> *School of Physics and Astronomy, University of Birmingham, Edgbaston, Birmingham, B15 2TT, England*

<sup>3</sup> *Laboratoire d'Astrophysique de Marseille, CNRS- Université Aix-Marseille, 38 rue Frédéric Joliot-Curie, 13388 Marseille Cedex 13, France*

<sup>4</sup> *California Institute of Technology, Mail Code 105–24, Pasadena, CA 91125, USA*

<sup>5</sup> *University of British Columbia, Department of physics and astronomy, 6224 Agricultural Rd., Vancouver, B.C., V6T 1Z1, Canada*

<sup>6</sup> *Harvard Center for Astrophysics and Las Cumbres Observatory Global Telescope Network Fellow*

<sup>7</sup> *Harvard-Smithsonian Center for Astrophysics, 60 Garden Street, Cambridge MA02138, USA*

<sup>8</sup> *Max-Planck-Institut für Astronomie, Königstuhl 17, 69117 Heidelberg, Germany*

<sup>9</sup> *Department of Physics, Università di Roma Tor Vergata, via della ricerca scientifica, 1, 00133 Roma, Italy*

<sup>10</sup> *Dark Cosmology Centre, Niels Bohr Institute, University of Copenhagen, Juliane Maries Vej 30, 2100 Copenhagen, Denmark*

<sup>11</sup> *Steward Observatory, University of Arizona, 933 North Cherry Avenue, Tucson, AZ 85721, USA*

<sup>12</sup> *Jet Propulsion Laboratory, Caltech, MS 169-327, Oak Grove Dr, Pasadena CA 91109, USA*

<sup>13</sup> *Johns Hopkins Dept. of Physics and Astronomy, Baltimore, MD 21218, USA*

\* *Marie-Curie fellow. E-mail: johan.richard@durham.ac.uk*

Accepted. Received; in original form

## ABSTRACT

We present a statistical analysis of a sample of 20 strong lensing clusters drawn from the Local Cluster Substructure Survey (LoCuSS), based on high resolution *Hubble Space Telescope* (*HST*) imaging of the cluster cores and follow-up spectroscopic observations using the Keck-I telescope. We use detailed parameterized models of the mass distribution in the cluster cores, to measure the total cluster mass and fraction of that mass associated with substructures within  $R \leq 250$  kpc. These measurements are compared with the distribution of baryons in the cores, as traced by the old stellar populations and the X-ray emitting intracluster medium. Our main results include: (i) the distribution of Einstein radii is log-normal, with a peak and  $1\sigma$  width of  $\langle \log_{10} \theta_E(z=2) \rangle = 1.16 \pm 0.28$ ; (ii) we detect an X-ray/lensing mass discrepancy of  $\langle M_{SL}/M_X \rangle = 1.3$  at  $3\sigma$  significance – clusters with larger substructure fractions displaying greater mass discrepancies, and thus greater departures from hydrostatic equilibrium; (iii) cluster substructure fraction is also correlated with the slope of the gas density profile on small scales, implying a connection between cluster-cluster mergers and gas cooling. Overall our results are consistent with the view that cluster-cluster mergers play a prominent role in shaping the properties of cluster cores, in particular causing departures from hydrostatic equilibrium, and possibly disturbing cool cores. Our results do not support recent claims that large Einstein radius clusters present a challenge to the CDM paradigm.

**Key words:** Gravitational lensing - Galaxies: clusters: general - Galaxies: clusters: individual (A521, A611, A773, A868, A1413, A1835, A2204, RXJ1720, RXJ2129, Z2701)

## 1 INTRODUCTION

The evolution of galaxy clusters with cosmic time is an important cosmological probe, as it traces the gravitational

growth of dark matter on large scales. In particular, the cluster mass function can be directly tested against cosmological models, as it is related to fundamental parameters

such as the matter density  $\Omega_m$ , the normalisation of the power spectrum  $\sigma_8$  (e.g. Schuecker et al. 2003; Smith et al. 2003), and the dark energy equation of state parameter  $w$ .

Commonly used probes of the mass of clusters at  $z \sim 0.1 - 0.5$  include the  $K$ -band luminosity (Lin et al. 2006), X-ray luminosity and temperature (e.g. Vikhlinin et al. 2006), Sunayev-Zeldovich effect (e.g. Nagai 2006; Bonamente et al. 2008), cluster kinematics (e.g. Blindert et al. 2004), and gravitational lensing (e.g. Bardeau et al. 2007; Smith et al. 2005; Okabe et al. 2009). Systematic errors in these various mass probes can be calibrated by an inter-comparison of results from the various methods. The pursuit of the most robust calibrations based on low redshift cluster samples is essential to achieve reliable results from future studies at higher redshift, and to control systematic uncertainties in cosmological experiments (Albrecht et al. 2006).

Gravitational lensing plays a central role in this effort, as it does not rely on assumptions about the symmetry or equilibrium properties of the cluster mass distribution, although parametrized lensed model implicitly assume, for instance, elliptical symmetry. Indeed, the highest quality measurements of the dark matter mass and substructure in low redshift clusters have been obtained through the combination of strong and weak gravitational lensing. The identification of background galaxies forming strong lensing arcs in cluster cores is a direct measurement of the enclosed mass within the Einstein radius  $\theta_E$ , providing an accurate normalisation of cluster mass models both in the core, and extending to larger radii (e.g. Kneib et al. 2003). The main caveats on lensing studies are that the lensing signal is sensitive to the mass distribution projected along the line of sight through the cluster, that the commonly used parametric models must by design assume a parametric form of the mass distribution, and that gravitational lensing may prove to be impractical in samples of more distant ( $z > 1$ ) cluster samples that are starting to be discovered (e.g. Rosati et al. 1999; Kurk et al. 2009).

Early joint lensing/X-ray cluster studies identified large discrepancies between total cluster masses obtained from the two methods (e.g. Miralda-Escude & Babul 1995). These discrepancies were subsequently eliminated, albeit within quite large uncertainties, in cool core clusters provided that a two phase gas model was used (Allen 1998; see also Smal et al. 1997). At a similar time, *HST* data started to become available for some clusters, allowing more precise strong lensing models to be constructed (e.g. Kneib et al. 1996; Tyson et al. 1998). More recent strong lensing studies of cluster mass distributions have generally continued to concentrate on detailed studies of spectacular individual strong lensing clusters based on deep multi-filter *HST* observations (e.g. Broadhurst et al. 2005; Limousin et al. 2007b; Richard et al. 2009). The interpretation of results from such studies, e.g. size of Einstein radii and shape of density profile, in the context of the general cluster population is inevitably problematic.

In contrast, Smith et al. (2005, hereafter Sm05) studied 10 X-ray selected clusters ( $L_{X,0.2-2.4\text{keV}} > 4.1 \times 10^{44} \text{erg s}^{-1}$ ) at  $z \simeq 0.2$  as a first step towards building large statistical samples of strong lensing clusters. Sm05 combined strong and weak lensing constraints from moderate depth *HST* observations with X-ray spectro-imaging from *Chandra*, and near-infrared photometry of cluster galaxies from UKIRT.

The main results included the first mass-observable scaling relations to employ lensing-based mass measurements for a well-defined sample; the only previous example employed a compilation of 6 clusters from the literature (Hjorth et al. 1998). The main limiting factor on Sm05's results were the small sample size, with just 5 of the 10 clusters containing spectroscopically confirmed strongly lensed galaxies.

The Local Cluster Substructure Survey (LoCuSS, PI: G. P. Smith) is an all-sky systematic survey of 165 X-ray luminous clusters at  $0.15 < z < 0.30$  selected from the *ROSAT* All-sky Survey catalogs (Ebeling et al. 1998, 2000; Böhringer et al. 2004). In addition to seeking to improve the statistical precision by enlarging the sample size of studies such as Sm05 and Bardeau et al. (2007), LoCuSS aims to incorporate new constraints on cluster baryons, most notably from observations of the Sunyaev-Zeldovich Effect (Carlstrom et al. 2002) to deliver a definitive local calibration of mass-observable scaling relations that will be useful for cluster cosmology, interpretation of high-redshift cluster samples, and probing the physics of gas heating and cooling in merging clusters at low redshift. More generally, LoCuSS aims to constrain the scatter in the baryonic properties of the local cluster population and to correlate the scatter with the recent hierarchical assembly history of the clusters, the latter being constrained by the lensing-based mass maps (Smith & Taylor 2008). A wide variety of studies are therefore underway, including wide-field weak-lensing analysis with Suprime-Cam on Subaru (Okabe et al. 2009), the first lensing-based mass- $Y_{SZ}$  relation (Marrone et al. 2009), and multiwavelength studies supported by space-based (*HST*, *Herschel*, *Chandra*, GALEX, *Spitzer*) as well as ground-based (Keck, VLT, Gemini, MMT, CTIO, KPNO, Palomar) facilities (e.g. Zhang et al. 2008; Haines et al. 2009a,b; Sanderson et al. 2009b; Smith et al. 2009b).

This paper presents a four-fold increase in the number of clusters with spectroscopically confirmed strong lensing clusters on Sm05. Such constraints remain critical within the overall context of the studies outlined above because strong-lensing offers precise constraints on the mass distribution in cluster cores ( $R \sim 100\text{kpc}$ ) which for example provide an invaluable constraint on small scales when trying to measure the shape of cluster density profiles in conjunction with wide-field weak-lensing data from Subaru. We compare the details of the central mass distributions (integrated mass and substructure fraction) obtained from the strong-lensing constraints with near-infrared and X-ray probes of the cluster baryons. We describe the data in §2, and present the strong-lensing analysis and models in §3. The main results on the mass and structure of the cluster cores are presented in §4 and summarized in §5. Throughout the paper, we use magnitudes quoted in the AB system, and a standard  $\Lambda$ -CDM model with  $\Omega_m = 0.3$ ,  $\Omega_\Lambda = 0.7$ , and  $H_0 = 70\text{km s}^{-1}\text{Mpc}^{-1}$ , whenever necessary. In this cosmology,  $1''$  is equivalent to  $3.3\text{kpc}$  at  $z = 0.2$ . We adopt the definition  $e = 1 - b/a$  of the ellipticity, where  $a$  and  $b$  are the semi-major and semi-minor axis of the ellipse, respectively.

## 2 OBSERVATIONS AND DATA REDUCTION

We present here the cluster sample and the relevant datasets used in our study. The strong lensing analysis relies on two

**Table 1.** Optical and near-infrared imaging observations of the new strong-lensing LoCuSS clusters.

Cluster	$\alpha_{\text{BCG}}$	$\delta_{\text{BCG}}$	$z$	<i>HST</i>			Near-infrared			
				PID	Camera/Filter	Depth ( $Z\sigma$ )	Camera	$J(Z\sigma)$	$K_S(Z\sigma)$	$K_S^*$
A 521 <sup>(a)</sup>	73.528753	-10.223605	0.2475	11312	WFPC2/F606W	27.0	WIRC	21.5	21.0	17.60
A 611	120.236680	36.056725	0.2850	9270	ACS/F606W	27.7	WIRC	21.0	20.9	17.85
A 773	139.472660	51.727024	0.2170	8249	WFPC2/F702W	27.6	WIRC	21.7	21.5	17.36
A 868	146.359960	-8.651994	0.1535	8203	WFPC2/F606W	27.5	ISPI	21.9	21.6	16.70
Z2701 <sup>(b)</sup>	148.204560	51.885143	0.2140	9270	ACS/F606W	27.7	WIRC	21.5	21.5	17.33
A 1413	178.824510	23.404451	0.1427	9292	ACS/F775W	27.3	WIRC	23.0	22.3	16.55
				9292	ACS/F850LP	26.7				
A 1835	210.258860	2.878532	0.2528	8249	WFPC2/F702W	27.7	ISPI	22.0	21.3	17.64
				10154	ACS/F850LP	27.3				
A 2204	248.195540	5.575825	0.1524	8301	WFPC2/F606W	26.4	FLAM.	22.1	21.9	16.68
RX J1720 <sup>(c)</sup>	260.041860	26.625627	0.1640	11312	WFPC2/F606W	26.9	WIRC	20.6	20.7	16.82
RX J2129 <sup>(d)</sup>	322.416510	0.089227	0.2350	11312	WFPC2/F606W	26.7	WIRC	21.7	21.7	17.51

<sup>(a)</sup> also known as RXC J0454.1–1014 <sup>(b)</sup> also known as ZwCl0949.6+5207 <sup>(c)</sup> RX J1720.1+2638 <sup>(d)</sup> RX J2129.6+0005

**Table 2.** Extended sample of 10 previously published spectroscopically-confirmed strong-lensing LoCuSS clusters

Cluster	$\alpha_{\text{BCG}}$	$\delta_{\text{BCG}}$	$z$	Strong-lensing reference
A 68	9.278626	9.156722	0.2546	Sm05, Richard et al. (2007); Smith et al. (2002)
A 383	42.014079	-3.529040	0.1883	Sm05, Smith et al. (2001); Sand et al. (2004)
A 963	154.264990	39.047228	0.2050	Sm05, Ellis et al. (1991)
A 1201	168.227080	13.435946	0.1688	Edge et al. (2003)
A 1689	197.872950	-1.341005	0.1832	Limousin et al. (2007b)
A 1703	198.771971	51.817494	0.2800	Richard et al. (2009)
A 2218	248.954604	66.212242	0.1710	Sm05, Kneib et al. (1996), Elíasdóttir et al. (2007)
A 2219	250.082380	46.711561	0.2281	Sm05
A 2390	328.403290	17.695740	0.2329	Jullo, PhD thesis
A 2667	357.914125	-26.084375	0.2264	Covone et al. (2006)

main ingredients: (a) the identification of multiply-imaged systems and (b) measurements of their spectroscopic redshifts. The former relies on high angular resolution *HST* imaging, while the latter is carried out using sensitive optical multi-object spectrographs on large aperture ground-based telescopes, in this case LRIS on the Keck-I 10-m telescope. We also use near-infrared photometry to select likely cluster galaxies based on the prominent red sequence of cluster galaxies in the  $J - K/K$  color-magnitude diagrams, that is largely insensitive to spectral type at  $z \simeq 0.2$ . These photometric catalogs are also used in the paper during the construction of the lens models (§3.2). Finally, we summarize the analysis of X-ray data available for the majority of these clusters, and which we later use as a comparison with the strong-lensing results (see §4).

## 2.1 Cluster sample

The sample in this article comprises the 10 clusters that we have spectroscopically confirmed as strong-lenses during our Keck observing campaign 2004–2008 (Table 1), plus a further 10 clusters within the LoCuSS sample that have been previously published (Table 2). To qualify for observations with Keck, a cluster must have been previously imaged with *HST* (79 clusters), and lie at  $\delta > -25^\circ$ . We note that some of the clusters with new strong-lensing models had previously been identified as candidate strong-lensing clusters:

- A 773 and A 1835 were included in Sm05’s sample however in the absence of spectroscopic confirmation, only weak-lensing constraints were used to construct the mass models.
- A 521 was studied by Maurogordato et al. (2000) using ground-based images. A giant arc feature was observed but spectroscopic follow-up attempts were unable to confirm its strong lensing origin.
- A 773, A 868, A 1835, A 2204 and Z2701 were part of the Sand et al. (2005) sample, who performed a systematic search for radial and tangential arc features in archival *HST* images of massive clusters. They identified radial arcs in A 773, A 1835, and A 2204.

## 2.2 Imaging data

### 2.2.1 HST imaging data

High resolution imaging data taken with the ACS or WFPC2 instrument on *HST* are available for each selected cluster in one or two bands, either through our dedicated LoCuSS program (GO-DD 11312, PI: G. P. Smith), or from the archive. These data are summarized in Table 1. In every case, one of the observed filters is located between the  $V$  and the  $I$  band, the most common being the F606W filter.

Each *HST* observation consists of several independent frames arranged in a dither pattern. These images were combined using the `multidrizzle` software with a final plate scale of  $0.05''$  (ACS) or  $0.1''$  (WFPC2). In the case of A 868, the observations comprise a mosaic of 6 WFPC2 pointings taken at different epochs. This mosaic was combined using

the relative astrometric shifts measured from bright objects in common between two adjacent pointings.

A careful visual inspection was performed on the reduced *HST* images by two of the authors (JR and GPS) to search for strong lensing features. A catalog of candidate multiple images was compiled by selecting highly sheared arc-like features, as well as objects displaying a very similar morphology and the characteristic symmetric effect of strong lensing (e.g., Fig. 2). The majority of these multiple images does not appear like arcs, but have a clumpy morphology, with multiple knots of star-formation. These lensed sources are not detected by automatic arc finding techniques (e.g. *Arcfinder*, Seidel & Bartelmann 2007), and therefore justify the use of a visual inspection of the images.

### 2.2.2 Near-infrared imaging data

$J$ - and  $K_S$ -band data were obtained between March 2003 and April 2007 on the following near-infrared instruments: WIRC on the Palomar-200in telescope, ISPI on the CTIO Blanco 4-m telescope, and FLAMINGOS on the Kitt Peak (KPNO) 4-m telescope. The properties of the data are summarized in Table 1. Observations in each filter comprised multiple frames with individual exposure times in the range 30 – 120sec. These images were combined using standard IRAF reduction techniques, full details will be provided in Smith et al. (in preparation), and flux-calibrated using the 2MASS source catalog. A dithering box of  $80''$  width was used in order to improve the photometry of the extended envelope of the BCGs. The field of view of the final dithered images is larger than  $8 \times 8$  arcmin<sup>2</sup>, centred on the Brightest Cluster Galaxy (BCG). This entirely covers the central  $R < 600$  kpc of each cluster (as measured from the BCG). We used the SExtractor (Bertin & Arnouts 1996) software to derive a photometric catalog of MAGAUTO magnitudes in the  $K_S$  band, as well as the  $J - K_S$  colours inside  $4.0''$  diameter apertures.

### 2.2.3 Photometric catalogs of cluster galaxies

In order to include galaxy-scale components in the strong-lens models (§3.2), it is important to perform a systematic selection of cluster members with their geometrical parameters (centroid  $\alpha_c$ ,  $\delta_c$ , ellipticity  $e_c$  and position angle  $\theta_c$ ) and total photometry in the  $K_S$  band. Indeed,  $K_S$  magnitudes are a more accurate proxy for stellar mass when making the assumption that light traces mass.

Cluster galaxies were selected from the near-infrared catalog using the red sequence technique on a  $J - K_S/K_S$  colour-magnitude diagram (Visvanathan & Sandage 1977). We adopted a limiting magnitude of  $K_S = 20$  (MAGAUTO) and a colour width of 0.3 magnitudes for the sequence (above 3 times the photometric uncertainties). The corresponding diagrams and colour selection regions are presented in Fig. 1. A final catalog of cluster members is obtained by correlating the *HST* and near-infrared photometric catalogs: in the central region, the geometrical parameters ( $\alpha_c$ ,  $\delta_c$ ,  $e_c$ ,  $\theta_c$ ) of cluster members are replaced by their more accurate measurements from the *HST* image.

As a sanity check, we plot the red sequence parameters used in our photometric selection ( $J - K_S$  colour at fixed

$K_S$ -band magnitude, and linear slope  $\kappa_{JK_S}$  of the colour-magnitude diagrams) as a function of the cluster redshift (Fig. 1, last 2 panels). The correlation between  $J - K_S$  at  $K_S = 18$  follows the expected colour of elliptical galaxies (using the empirical model from Coleman et al. (1980), while the slope  $\kappa_{JK_S}$  is scattered around an average value  $\kappa_{JK_S} = -0.028$ , compatible with similar measurements obtained by Stott et al. (2009) in this range of cluster redshifts.

We estimated  $K_S^*$ , the  $K_S$  band magnitude of an  $L^*$  galaxy, following the results from Lin et al. (2006). They show that the evolution of  $K_S^*$  with cluster redshift is best reproduced by a single burst model at  $z_{form} = 1.5$  from Bruzual & Charlot (2003), assuming a Salpeter initial mass function and solar metallicity. Their best fit  $K_S^*(z)$  values are reported in the final column of Table 1. Our current selection down to  $K_S = 20$  enables us to select cluster members down to  $\sim 0.1L^*$ . Since the fraction of fainter cluster members not included in our selection contribute to less than 1% of the total  $K$ -band luminosity, this selection does not affect our results on the  $K$ -band properties in the entire sample.

## 2.3 Spectroscopic data

### 2.3.1 Observing strategy

We used the Low Resolution Imager and Spectrograph (LRIS, Oke et al. 1995) on the Keck-I telescope to perform long-slit and multi-slit observations of the clusters. The spectroscopic data used in the current paper is the outcome of 6 different observing runs between 2004 and 2008, which are summarized in Table 3.

We designed multi-slit masks containing  $\sim 30$  slits of  $1.0''$  width to include as many of the candidate multiple systems as possible, with a few tilted slits following the geometry of long arcs. In the case of fainter or less reliable identifications, several images of the same system were observed in separate slits. Additional slits in the mask included faint galaxies with unknown redshifts, bright infrared sources selected at  $24\mu\text{m}$ , or cluster members.

The dichroic/grism/grating combinations listed in Table 3 to ensure a high throughput over the wavelength range 3500 to 9500 Å and good spectral resolution (Table 3) in the red to resolve OH skylines as well as [OII] emission line doublets in the redshift range 0.85 – 1.50. The total exposure time varied between 1 and 3 hours per mask, depending on the seeing conditions and the detection of strong emission lines when looking over a first reduction of the data at the telescope.

### 2.3.2 Data reduction

The data were reduced using the Python version of the Kelson (2003) reduction scripts, which offer the advantage of processing the images in their distorted framework. This helps to reduce noise correlations, in particular for the case of tilted slits. We performed standard reduction steps for bias removal, flat-field correction, wavelength calibration, sky subtraction, and cosmic-ray rejection, and used observations of spectroscopic standard stars obtained on the same nights to derive the flux calibration.

The extracted spectra of objects used in the present paper are shown in Fig. A1 (appendix). These spectra show

**Figure 1.**  $J - K_S$  vs  $K_S$  colour-magnitude diagrams for each observed cluster, showing the red sequence selection of cluster members (red dots). The photometric selection used is shown as delimited by the solid box (see text for details). The last two panels show the red sequence  $\kappa_{JK_S}$  parameters (intercept at  $K_S = 18$  and slope  $\kappa_{JK_S}$ ) as a function of cluster redshift. The solid line gives the expected colours of an elliptical galaxy, and the dashed line marks the average slope  $\kappa_{JK_S}$  for the sample.

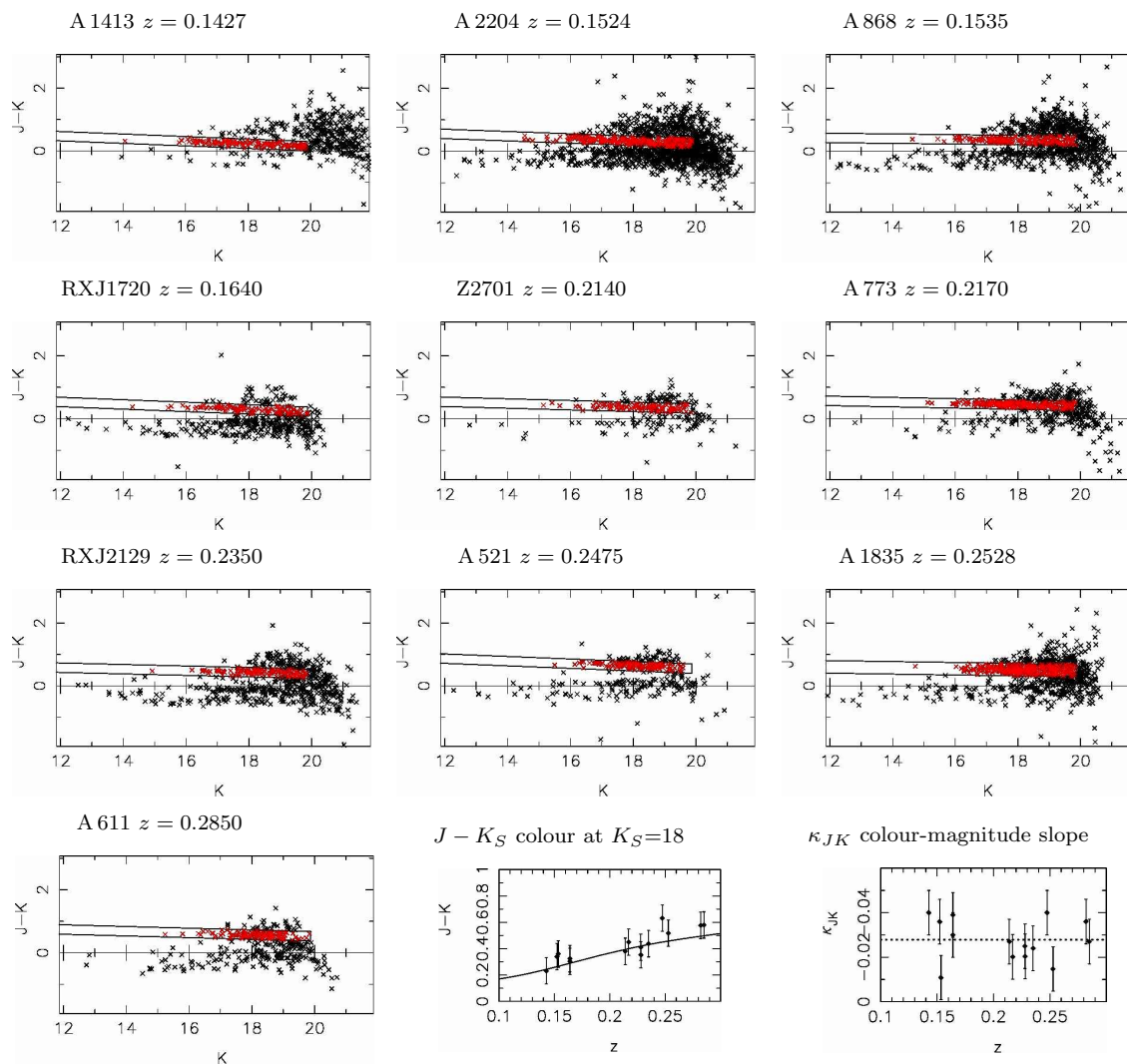


**Table 3.** Summary of the Keck/LRIS spectroscopic data.

Cluster	Date	Config	$N_{\text{slits}}$	Grism	Grating[ $\lambda_c$ ]	Dichroic	$T_{\text{exp}}$ (ks)	Seeing	Standard star
A 521	Feb 2007	MOS	18	400/3400	900/5500 [6320]	560	3.8	1.1''	Feige 92
				400/3400	831/8200 [8100]	560	3.6	1.1''	Feige 92
A 611	Nov 2006	LS	1	600/4000	400/8500 [7970]	560	4.5	0.9''	Feige 110
	Jan 2007	LS	1	600/4000	400/8500 [7970]	560	1.8	1.3''	Feige 34
A 773	Feb 2007	MOS	26	400/3400	900/5500 [6400]	560	3.6	1.0''	Feige 92
				400/3400	831/8200 [8070]	560	3.6	1.0''	Feige 92
A 868	May 2008	MOS	36	300/5000	600/7500 [8100]	680	5.4	0.7''	BD+33-2642
Z2701	May 2008	MOS	22	300/5000	600/7500 [8100]	680	3.6	1.0''	BD+33-2642
A 1413	Feb 2004	LS	1	600/4000	400/8500 [7640]	560	5.4	0.9''	
A 1835	March 2005	MOS	36	400/3400	600/7500 [6850]	560	7.2	0.7''	G138-31
A 2204	May 2008	MOS	37	300/5000	600/7500 [8100]	680	3.6	0.7''	BD+33-2642
RXJ1720	May 2008	MOS	21	300/5000	600/7500 [8100]	680	5.4	0.9''	BD+33-2642
				400/3400	600/7500 [8100]	680	5.4	0.9''	BD+33-2642
RXJ2129	May 2008	MOS	22	300/5000	600/7500 [8100]	680	5.4	1.1''	BD+33-2642

**Table 4.** Properties of the multiple imaged systems. Redshift values quoted with brackets are predictions from the lensing model. The last two columns give the observed *HST* magnitudes and linear magnification factor predicted by the lens model.

Cluster / Multiple	$\alpha$	$\delta$	$z$	Reference	<i>HST</i>	$\mu$ (mags)	$\mu$ (linear)
A 521					(F606W)		
1.1 <sup>a</sup>	73.526932	-10.223421	1.043±0.01	[OII], CII, FeII	21.49 ± 0.04	1.76±0.10	5.1±0.5
1.2	73.527544	-10.222524	1.043±0.01	CII, FeII	21.32 ± 0.04	1.71±0.10	4.8±0.4
1.3	73.529391	-10.221431	1.043±0.01	[OII]	21.57 ± 0.20	0.98±0.10	2.5±0.2
A 611					(F606W)		
1.1 <sup>a</sup>	120.23219	36.061593			24.58 ± 0.03	1.38±0.11	3.6±0.4
1.2	120.24171	36.055210	2.06 ± 0.02	CIII, CIV	23.87 ± 0.05	2.52±0.30	10.2±2.8
1.3	120.24103	36.058273	2.06 ± 0.02	CIII, CIV	22.80 ± 0.10	1.95±0.18	6.0±1.0
1.4	120.23555	36.054247			24.98 ± 0.04	0.79±0.06	2.1±0.1
1.5	120.23589	36.054887			25.46 ± 0.05	1.0±0.07	2.5±0.2
2.1	120.23716	36.061183	0.908 ± 0.005	[OII]	23.26 ± 0.02	2.47±0.29	9.7±2.6
2.2	120.24046	36.059825	0.908 ± 0.005	[OII]	23.26 ± 0.09	1.10±0.08	2.8±0.2
2.3	120.24206	36.057539	0.908 ± 0.005	[OII]	23.17 ± 0.14	2.48±0.29	9.8±2.6
3.1	120.23554	36.060897	[2.5 <sup>+0.5</sup> <sub>-0.2</sub> ]		24.42 ± 0.03	4.08±1.27	42±15
3.2	120.23739	36.060653			25.05 ± 0.06	2.04±0.19	6.5±1.2
3.3	120.24311	36.053638			25.94 ± 0.08	1.38±0.11	3.6±0.4
3.4	120.23407	36.055807			25.63 ± 0.07	1.39±0.11	3.6±0.4
4.1	120.24182	36.056242	2.59 ± 0.01	Ly $\alpha$	27.14 ± 0.19	4.35±1.62	55±17
4.2	120.23193	36.062088			27.67 ± 0.19	1.26±0.09	3.2±0.2
A 773					(F702W)		
1.1	139.48925	51.729656	2.300±0.005	Ly $\alpha$ , SiII, SiIV, CIV	22.95 ± 0.02	2.69±0.35	11.9±3.8
1.2	139.48920	51.724870	2.300±0.005		23.03 ± 0.02	3.0±0.5	16.0±6.9
1.3	139.48351	51.741593			23.47 ± 0.02	1.57±0.13	4.2±0.5
2.1	139.46920	51.732350	3.84±0.01	Ly $\alpha$	23.85 ± 0.06	2.42±0.27	9.3±2.3
2.2	139.48762	51.716864			23.58 ± 0.06	1.18±0.09	3.0±0.3
3.1	139.49535	51.728050	1.010±0.005	[OII]	23.09 ± 0.05	2.0±0.2	6.1±1.0
3.2	139.49501	51.728985	1.010±0.005	[OII]	21.54 ± 0.05	2.0±0.2	6.1±1.0
A 868					(F606W)		
1.1	146.36459	-8.6481919	0.551±0.002	[OII],[OIII]	22.60 ± 0.03 <sup>(b)</sup>	3.29±0.61	36±7.8
1.2	146.36474	-8.6490159	0.551±0.002	[OII],[OIII]	22.60 ± 0.03 <sup>(b)</sup>	2.28±0.24	19±4.7
1.3	146.36554	-8.6502853	0.551±0.002		23.50 ± 0.05	2.64±0.34	23.±4.1
Z2701					(F606W)		
1.1	148.20940	51.885620	1.163	[OII]	23.73 ± 0.03	5.32±0.98	20.7±6.1
1.2	148.20708	51.883841			24.22 ± 0.03	3.90±0.88	8.2±1.8
1.3	148.20087	51.882325	1.163	[OII]	24.34 ± 0.03	2.62±0.33	11.4±3.7
2.1	148.21056	51.884031	[2.5 <sup>+0.2</sup> <sub>-0.3</sub> ]		25.05 ± 0.08	3.73±0.92	130±60
2.2	148.20988	51.883375			24.99 ± 0.08	3.90±0.88	36.±9
2.3	148.20083	51.880880			25.52 ± 0.05	2.62±0.33	11.2±3.4
A 1413					(F775W)		
1.1	178.82496	23.412185	2.726±0.003	Ly $\alpha$ , SiII	23.16 ± 0.06	3.73±0.92	31.±6.
1.2	178.82328	23.412089	2.726±0.003	Ly $\alpha$ , SiII	22.79 ± 0.08	5.00±2.95	100±27
2.1	178.82855	23.399205	2.030±0.004	Ly $\alpha$ , SiII	22.90 ± 0.16	2.37±0.26	8.9±2.1
2.2	178.82591	23.398715	2.030±0.004	Ly $\alpha$ , SiII	22.99 ± 0.23	2.94±0.44	15±6
2.3	178.81985	23.399441			23.82 ± 0.09	2.50±0.30	10±2.8
3.1	178.82933	23.406898	1.20±0.01	[OII]	23.03 ± 0.06	1.28±0.10	3.3±0.3
3.2	178.82391	23.407396	1.20±0.01	[OII]	23.64 ± 0.21	1.54±0.12	4.1±0.5
3.3	178.81981	23.405955	1.20±0.01	[OII]	22.84 ± 0.13	1.33±0.10	3.4±0.3
4.1	178.82940	23.409414	[2.9 <sup>+0.3</sup> <sub>-0.2</sub> ]		25.47 ± 0.05	1.30±0.10	3.3±0.3
4.2	178.82263	23.409657			24.50 ± 0.03	2.07±0.20	6.7±1.2
4.3	178.82007	23.408814			24.57 ± 0.03	1.95±0.18	6.0±1.0

<sup>(a)</sup> location of the brightest knot in the image. <sup>(b)</sup> Photometry is the sum of 1.1 and 1.2 images

Lyman- $\alpha$  (in absorption or emission) and/or additional ultraviolet absorption lines, or the resolved [OII] doublet. For some faint multiple systems observed in different slits, redshift measurements were derived after stacking the relevant exposures. The average redshift value is obtained from the

peaks of the main spectral features identified, while the corresponding error is taken from the spectral dispersion. Additional uncertainties generated by the accuracy of the relative and absolute wavelength calibrations, about 1.1 and 1.5

**Table 4** Continued.

Cluster / Multiple	$\alpha$	$\delta$	$z$	Reference	<i>HST</i>	$\mu$ (mags)	$\mu$ (linear)
A 1835					(F850LP)		
1.1	210.26573	2.8706065	$[2.5^{+0.2}_{-0.2}]$		$24.28 \pm 0.12$	$2.15 \pm 0.22$	$7.2 \pm 1.5$
1.2	210.26403	2.8693007			$23.64 \pm 0.20$	$4.33 \pm 1.60$	$54 \pm 16$
1.3	210.24740	2.8698812			$25.12 \pm 0.25$	$0.83 \pm 0.06$	$2.1 \pm 0.1$
2.1	210.26614	2.8741625	$[1.3^{+0.1}_{-0.1}]$		$23.28 \pm 0.28$	$1.60 \pm 0.13$	$4.4 \pm 0.5$
2.2	210.26358	2.8714121			$22.87 \pm 0.29$	$0.42 \pm 0.04$	$1.5 \pm 0.05$
2.3	210.24824	2.8717531			$25.40 \pm 0.30$	$0.85 \pm 0.07$	$2.2 \pm 0.1$
3.1	210.26326	2.8849801	$[3.0^{+0.2}_{-0.1}]$		$25.63 \pm 0.07$	$2.31 \pm 0.25$	$8.4 \pm 1.9$
3.2	210.26278	2.8852175			$25.28 \pm 0.06$	$2.66 \pm 0.34$	$11.6 \pm 3.6$
3.3	210.24374	2.8775381			$25.87 \pm 0.07$	$1.87 \pm 0.17$	$5.6 \pm 0.9$
4.1	210.26382	2.8846758	$[2.3^{+0.1}_{-0.1}]$		$24.70 \pm 0.04$	$1.96 \pm 0.18$	$6.1 \pm 1.0$
4.2	210.26073	2.8858319			$25.41 \pm 0.07$	$3.15 \pm 0.54$	$17.4 \pm 8.0$
4.3	210.24435	2.8781489			$25.08 \pm 0.13$	$0.83 \pm 0.06$	$2.1 \pm 0.1$
5.1	210.25984	2.8824075	2.6	<i>Ly<math>\alpha</math></i> (a)	$23.44 \pm 0.03$	$0.67 \pm 0.05$	$1.8 \pm 0.1$
5.2	210.24484	2.8721518	2.6	<i>Ly<math>\alpha</math></i> (a)	$23.90 \pm 0.02$	$0.69 \pm 0.06$	$1.9 \pm 0.1$
5.3	210.25921	2.8792670			$26.04 \pm 0.18$		
6.1	210.26165	2.8775836	$[3.6^{+1.2}_{-1.4}]$		$25.77 \pm 0.09$	$0.99 \pm 0.07$	$2.5 \pm 0.2$
6.2	210.26131	2.8777493			$25.43 \pm 0.06$	$0.80 \pm 0.06$	$2.1 \pm 0.2$
7.1	210.25395	2.8731863	$2.070 \pm 0.004$	<i>Ly<math>\alpha</math>, SiIII, SiIV, CIV</i>	$22.28 \pm 0.04$	$4.86 \pm 2.59$	$88 \pm 30$
7.2	210.25421	2.8803387			$23.96 \pm 0.05$	$4.00 \pm 1.18$	$40 \pm 21$
7.3	210.27108	2.8801023			$25.02 \pm 0.05$	$0.86 \pm 0.07$	$2.2 \pm 0.1$
A 2204					(F606W)		
1.1	248.19665	5.5781303	$1.06 \pm 0.01$	[OII] (b)	$23.60 \pm 0.12$	$1.25 \pm 0.09$	$3.2 \pm 0.3$
1.2	248.19457	5.5689343	$1.06 \pm 0.01$	[OII]	$22.61 \pm 0.03$	$0.85 \pm 0.06$	$2.2 \pm 0.1$
1.3	248.19603	5.5779196			$23.70 \pm 0.15$	$0.53 \pm 0.05$	$1.6 \pm 0.08$
RXJ1720					(F606W)		
1.1	260.04314	26.624351	$2.136 \pm 0.005$	<i>MgII</i>	$22.74 \pm 0.05$ (c)	$3.16 \pm 0.54$	$18.4 \pm 9.1$
1.2	260.04247	26.624155	$2.136 \pm 0.005$	<i>MgII</i>	$22.74 \pm 0.05$ (c)	$1.54 \pm 0.12$	$4.1 \pm 0.5$
1.3	260.03779	26.626930			$24.85 \pm 0.08$	$0.91 \pm 0.07$	$2.3 \pm 0.2$
1.4	260.04285	26.626111			$24.41 \pm 0.07$	$1.33 \pm 0.10$	$3.4 \pm 0.3$
RXJ2129					(F606W)		
1.1	322.42040	0.088305	$1.965 \pm 0.005$	<i>SiIV, SiII, CIV</i>	$23.41 \pm 0.03$	$4.30 \pm 1.56$	$52 \pm 17$
1.2	322.42018	0.089722	$1.965 \pm 0.005$	<i>SiIV, SiII, CIV</i>	$23.05 \pm 0.02$	$2.33 \pm 0.25$	$8.6 \pm 2.0$
1.3	322.41798	0.093250			$24.74 \pm 0.06$	$2.23 \pm 0.23$	$7.8 \pm 1.6$

(<sup>a</sup>) Dannerbauer et al., in preparation (<sup>b</sup>) See also Wilman et al. (2006) (<sup>c</sup>) Photometry is the sum of 1.1 and 1.2 images

Å, respectively, were quadratically added to yield the final redshift errors. The redshifts are listed in Table 4.

## 2.4 X-ray observations

X-ray properties of the LoCuSS clusters have been determined for 18/20 clusters from *Chandra* archival observations, which were reduced and analyzed as described in Sanderson et al. (2009a) following the methods developed by Sanderson & Ponman (2009). Annular gas temperature and density profiles were derived and fitted with the phenomenological cluster model of Ascasibar & Diego (2008), to determine the total cluster mass profile. These models are based on the Hernquist (1990) profile, which has the advantage of yielding convergent three- and two-dimensional mass measurements. The latter is particularly helpful when comparing lensing and X-ray based measurements of the projected mass within  $R < 250$  kpc (see §2.4).

The X-ray models were also used to measure the gradient of the logarithmic gas density profile at  $0.04r_{500}$  ( $\alpha$ ; Vikhlinin et al. 2007), which quantifies the strength of cooling in the core (Vikhlinin et al. 2007; Sanderson et al. 2009a). Core-excluded mean temperatures for the clusters

were also measured in the range  $0.15 - 0.2r_{500}$ , according to the procedure outlined in Sanderson et al. (2009b). We classify clusters as hosting a cool core if the slope of the gas density profile is  $\alpha < -0.85$ . This matches the range of  $\alpha$  displayed by clusters that contain an H $\alpha$  emitting BCG in Sanderson et al. (2009a). Under this definition, 8/18 clusters as cool core clusters, corresponding to  $44 \pm 14\%$  where the error bar is a binomial uncertainty following Gehrels (1986). We also classify clusters as “disturbed” if the offset between the X-ray centroid and the BCG is  $> 0.01r_{500}$ , this identifies all except 3 of the clusters containing an H $\alpha$  emitting BCG in Sanderson et al. (2009a, see their Fig. 5). This yields a fraction of  $67^{+12}_{-15}\%$  of the sample that are classified as undisturbed. All cool core clusters are also classified as undisturbed, however 4 non-cool core clusters are also classified as undisturbed. The resulting X-ray properties are given in Table 5.

## 3 STRONG-LENSING ANALYSIS

We now describe the multiply-imaged galaxies used to constrain mass models of the 10 new strong-lensing clusters

**Table 5.** Summary of Chandra X-ray properties for the Keck sample (1st half) and the extended sample (2nd half)

Cluster	$L_X^a$	ID <sup>b</sup>	Temperature <sup>c</sup> (keV)	$r_{500}$ (kpc)	$M_X(R < 250\text{kpc})$ ( $10^{13} M_\odot$ )	$\alpha^d$	Cool core?	Offset <sup>e</sup> (kpc)	Disturbed?
A 521	9.45	901	$7.08^{+1.15}_{-1.53}$	$921 \pm 26$	$8.5 \pm 0.5$	$-0.10 \pm 0.29$	No	37	Yes
A 611	8.05	3194	$7.94^{+1.07}_{-1.22}$	$1342 \pm 140$	$20.6 \pm 1.9$	$-0.70 \pm 0.04$	No	1	No
A 773	7.74	5006	$7.50^{+0.87}_{-1.01}$	$1358 \pm 45$	$18.0 \pm 1.1$	$-0.40 \pm 0.05$	No	20	Yes
Z 2701	6.32	3195	$5.08^{+0.41}_{-0.43}$	$1271 \pm 300$	$15.0 \pm 4.1$	$-0.88 \pm 0.12$	Yes	3	No
A 1413	7.80	5003	$6.90^{+0.32}_{-0.35}$	$1296 \pm 28$	$18.4 \pm 0.5$	$-0.68 \pm 0.04$	No	2	No
A 1835	22.80	6880	$9.82^{+0.43}_{-0.44}$	$1506 \pm 57$	$24.6 \pm 1.0$	$-1.17 \pm 0.05$	Yes	5	No
A 2204	12.57	7940	$9.64^{+0.54}_{-0.54}$	$1420 \pm 59$	$23.8 \pm 1.4$	$-1.22 \pm 0.04$	Yes	8	No
RX J1720	9.54	4361	$7.96^{+0.97}_{-0.82}$	$1349 \pm 71$	$19.2 \pm 1.1$	$-1.06 \pm 0.04$	Yes	6	No
RX J2129	11.00	552	$8.27^{+1.48}_{-1.87}$	$1155 \pm 33$	$16.1 \pm 1.1$	$-1.09 \pm 0.03$	Yes	6	No
A 868	3.46	N/A							
A 68	8.81	3250	$8.89^{+1.76}_{-3.37}$	$941 \pm 56$	$11.9 \pm 1.8$	$-0.25 \pm 0.02$	No	52	Yes
A 383	5.27	2320	$5.01^{+0.43}_{-0.47}$	$1014 \pm 47$	$12.1 \pm 1.0$	$-1.09 \pm 0.03$	Yes	2	No
A 963	6.16	903	$6.73^{+0.52}_{-0.77}$	$1210 \pm 39$	$16.9 \pm 0.7$	$-0.68 \pm 0.05$	No	6	No
A 1201	3.72	4216	$5.56^{+0.82}_{-0.61}$	$1016 \pm 30$	$10.7 \pm 0.6$	$-0.65 \pm 0.13$	No	11	Yes
A 1689	16.27	5004	$8.86^{+0.68}_{-0.88}$	$1451 \pm 23$	$25.7 \pm 1.0$	$-0.77 \pm 0.03$	No	3	No
A 2218	5.51	1666	$7.17^{+0.51}_{-0.58}$	$1216 \pm 34$	$16.0 \pm 0.6$	$-0.33 \pm 0.03$	No	41	Yes
A 2219	12.07	896	$11.52^{+0.8}_{-0.9}$	$1786 \pm 149$	$26.9 \pm 1.4$	$-0.31 \pm 0.03$	No	28	Yes
A 2390	12.69	4193	$9.78^{+0.55}_{-0.56}$	$1437 \pm 68$	$20.0 \pm 1.0$	$-0.94 \pm 0.02$	Yes	2	No
A 2667	15.78	2214	$5.66^{+0.62}_{-0.85}$	$1243 \pm 115$	$14.1 \pm 1.6$	$-0.89 \pm 0.05$	Yes	3	No
A 1703	8.66	N/A							

<sup>a</sup> X-ray luminosity in the 0.1 – 2.4keV band from *ROSAT* (Ebeling et al. 1998, 2000; Böhringer et al. 2004). <sup>b</sup> *Chandra* observation identifier. <sup>c</sup> Measured between 0.15 and  $0.2r_{500}$  (see Sanderson et al. 2009b). <sup>d</sup> Logarithmic slope of the gas density profile at  $0.04r_{500}$  (see Vikhlinin et al. 2007; Sanderson & Ponman 2009). <sup>e</sup> X-ray centroid/BCG offset from Sanderson et al. (2009a). Errors are  $1\sigma$ .

(§3.1), and the methods used to construct the models themselves (§3.2).

### 3.1 Multiple images and spectroscopic redshifts

The multiple-image constraints used for each cluster are described below, and summarized in Table 4, including their astrometry, photometry and available spectroscopic redshifts. The locations of the multiple images are also marked in Fig. 2. The naming convention for multiple images in a given cluster is the following: (1.1, 1.2, 1.3, ...) are individual images in system 1, (2.1, 2.2, 2.3,...) in system 2, and so on.

#### A 521

The WFPC2 observations revealed a triply-imaged face-on spiral just  $6''$  from the BCG, and containing many individual knots of star formation. The clear symmetry between these knots (marked A to E in Fig. 2) confirms a strong-lensing system of 3 images, which we measure to be at  $z = 1.034$  from  $[OII]$  emission and UV absorption lines. We included the 3 brightest knots of each image as 9 individual constraints for the mass modeling. The system was previously identified by Maurogordato et al. (1996) using CFHT ground-based imaging. However the poor angular resolution of their data prevented them from identifying it as strongly-lensed, and subsequent spectroscopy was also inconclusive (Maurogordato et al. 2000).

#### A 611

We identify 4 systems, the first of which (1.1 to 1.5) clearly appears as 5 images of identical clumpy morphology, each of them composed of 5 individual knots (A to E) of star formation. We obtained a spectroscopic redshift for 1.2 and 1.3, showing identical features of a  $z = 2.06$  galaxy. The locations of the radial counter-images (1.4 and 1.5) are confirmed by a preliminary mass model. The second system (2.1 to 2.3) appears as a giant arc to the North-East of the BCG, for which we derive  $z = 0.908$  from strong  $[OII]$  emission. This giant arc is clearly affected by the presence of cluster substructure, with significant changes of curvature close to individual galaxies. The third system (3.1 to 3.4) was identified thanks to the symmetry between 3.1 and 3.2. The mass model predicts counter images that we identify as 3.3 and 3.4. Finally, a very faint arc (4.1) serendipitously falling in one of the slits was confirmed at  $z = 2.54$  with strong Lyman- $\alpha$  emission. The mass model confirmed it is located on the  $z = 2.5$  critical line, and predicts the counter image that we identify as 4.2.

#### A 773

We identify 3 multiply imaged systems in this cluster. System 1 is a triply-imaged system with a clear symmetry between components 1.1 and 1.2. We derived a redshift  $z = 2.3$  for both images and identify the counter-image 1.3 with help from the mass model. The second system (2.1 and 2.2) is a radial image and counter-image at  $z = 3.84$  from strong Ly $\alpha$  emission. Finally, we found a spectroscopic redshift  $z = 1.0$



for the third system (3.1 and 3.2) curving around one of the cluster galaxies.

#### A 868

A giant arc containing three bright images (1.1 to 1.3) is clearly found around the second brightest galaxy to the north-east of the BCG. We derive its redshift at  $z = 0.551$  from the combination of  $[OII]$  and  $[OIII]$  emissions. The curvature of this arc suggests it is strongly affected by a secondary mass component, as well as the main component centred on the BCG.

#### Z2701

We identify a first system (1.1 to 1.3) as three compact images  $\sim 10''$  from the BCG, confirmed to be at  $z = 1.163$ . A second system is formed by two faint symmetric arcs (2.1 and 2.2), for which the mass model predicts a counter-image identified as 2.3.

#### A 1413

The two-filter ACS data enable 4 multiply-imaged galaxies to be identified from their colours and morphologies, three of them having spectroscopic redshifts between  $z = 1.17$  and  $z = 2.77$ , from  $[OII]$  or Lyman- $\alpha$  in emission. System 1 is a bright fold arc to the north, where we identify two bright knots as 1.1 and 1.2. The three other systems are triply-imaged with clear mirror symmetry.

#### A 1835

Several studies have previously identified strongly-lensed arcs in this cluster (Schmidt et al. 2001; Sand et al. 2005, Sm05) however to date spectroscopic redshifts have not been measured for any of these background galaxies, thereby limiting the precision of previous attempts to model the mass distribution in this cluster. We report redshift measurements for two systems: one of them is a triple system (labelled 5) discovered during a narrow-band search for Lyman- $\alpha$  emitters at  $z = 2.5$  (Dannerbauer et al., in preparation), as two objects with similar morphologies and strong Ly- $\alpha$  emission. A radial counter image (5.3) is predicted close to the BCG. The second is a pair of merging images (system 7) measured at  $z = 2.07$ , for which we identify two counter images 7.2 and 7.3. A 4th image 7.4 is predicted very close to the BCG but the light of the BCG prevents a reliable identification. Finally, we checked that the submillimetre sources J1/J2 discussed by Smail et al. (2005) at  $z = 2.56$  are indeed predicted by the mass model to be singly-imaged.

#### A 2204

The redshift of a radial arc (1.1 and 1.2) was measured to be  $z = 1.0$  from strong  $[OII]$  emission during an IFU observation of the central galaxy with the VIMOS instrument (Wilman et al. 2006). We confirm this redshift independently, and find the same redshift for 1.3, which our mass model predicted to be the counter image.

#### RX J1720

This cluster is constrained by a giant arc (1.1 and 1.2) curving around the BCG, with a spectroscopic redshift  $z = 2.136$  from the magnesium doublet. We identify two counter images (1.3 and 1.4) with help from the mass model.

#### RX J2129

Two compact sources with mirror symmetry (1.1 and 1.2) have been identified  $z = 1.965$  from UV absorption lines, and the location of the counter image 1.3 was identified with the mass model.

### 3.2 Cluster mass models

We have used Lenstool<sup>1</sup> (Kneib 1993; Jullo et al. 2007) to reconstruct the distribution of mass in the cluster cores, which is described as a superposition of analytic mass components that account for both cluster- and galaxy-scale mass, following Sm05. We use all the multiple-image systems described in the previous section and Table 4 as model constraints, using spectroscopic redshifts whenever available. The main differences between these models and those of Sm05 are that unknown multiple-image redshifts are free parameters in the models, and two different parameterisations are used for the smooth cluster-scale mass components (§3.2.1), and parameter space is explored using the Bayesian MCMC sampler that is now available within Lenstool (§3.2.4). In common with Sm05 and other studies of strong-lensing clusters by our group, (e.g. Kneib et al. 1996; Smith et al. 2001, 2002; Richard et al. 2007; Limousin et al. 2007b, 2008; Richard et al. 2009; Smith et al. 2009a), the mass modelling is an iterative process, as we first produce a rudimentary mass model, based on the most reliable constraints, and then gradually incorporate additional constraints.

#### 3.2.1 Cluster-scale mass components

The mass distribution of cluster cores within the strong-lensing region is generally well-described by a smooth elliptical profile centred near the BCG. As a starting point in our analysis, we try to reproduce the strong lensing constraints using a double pseudo-isothermal elliptical mass distribution (dPIE, also known as a smoothly truncated PIEMD, Elíasdóttir et al. 2007). The dPIE profile, which was also used in Sm05, is characterized by its central position, position angle and ellipticity, the central velocity dispersion  $\sigma_0$  and two characteristic radii: a core radius  $r_{\text{core}}$  and a cut radius  $r_{\text{cut}}$ . In an  $(x, y)$  coordinate system oriented along the angle  $\theta$  of the ellipse, the surface mass density takes the form:

$$\Sigma(x, y) = \frac{\sigma_0^2}{2G} \frac{r_{\text{cut}}}{r_{\text{cut}} - r_{\text{core}}} \left[ \frac{1}{(r_{\text{core}}^2 + \rho^2)^{1/2}} - \frac{1}{(r_{\text{cut}}^2 + \rho^2)^{1/2}} \right] \quad (1)$$

with  $\rho^2 = [(2-e)(x-x_c)/2]^2 + [(2-e)(y-y_c)/(2-2e)]^2$ , and  $(x_c, y_c)$  is the centre of the mass distribution (see also Sm05).

<sup>1</sup> Publicly available at <http://www.oamp.fr/cosmology/lenstool>

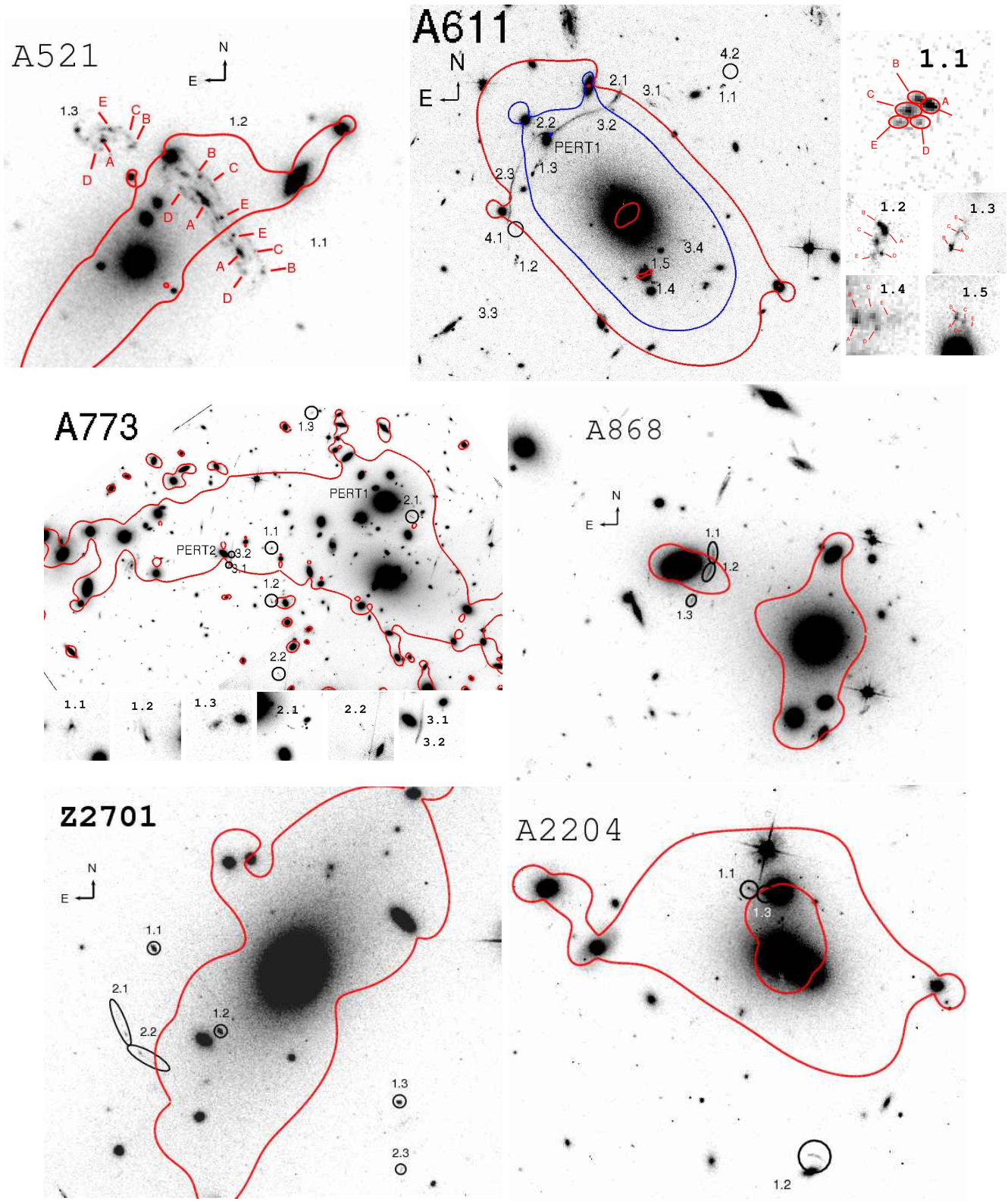


**Figure 2.** Multiple-image identifications and critical line at redshift 1.0 (A 521), 0.91 and 2.1 (A 611), 2.3 (A 773), 0.55 (A 868), 1.2 (Z2701) and 1.1 (A 2204). Individual knots used as independent constraints are marked in A 521 and A 611.

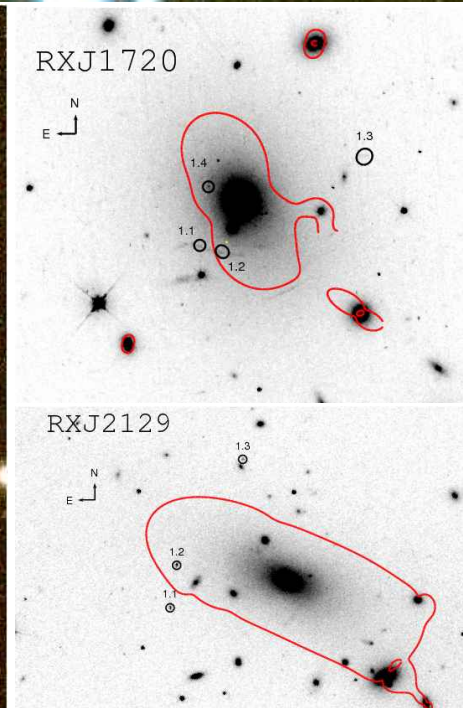
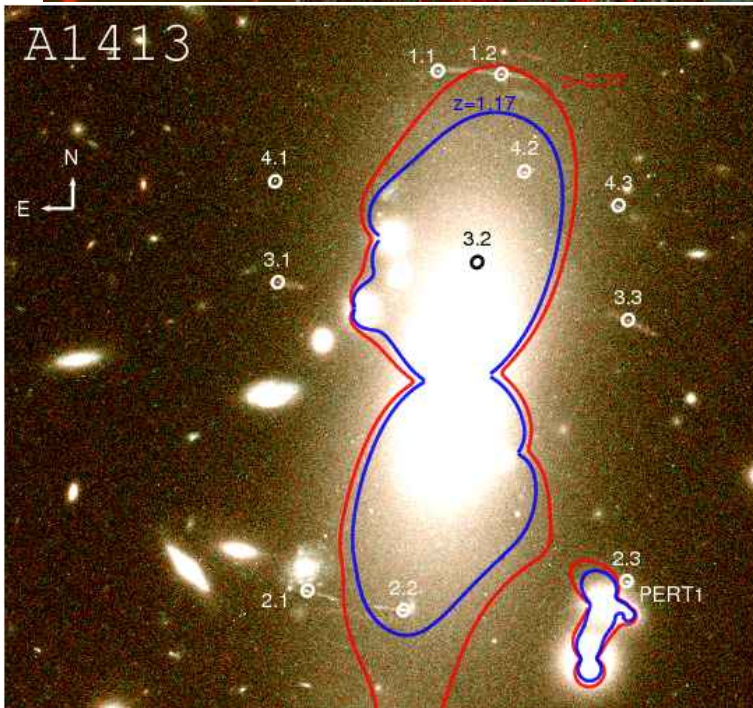
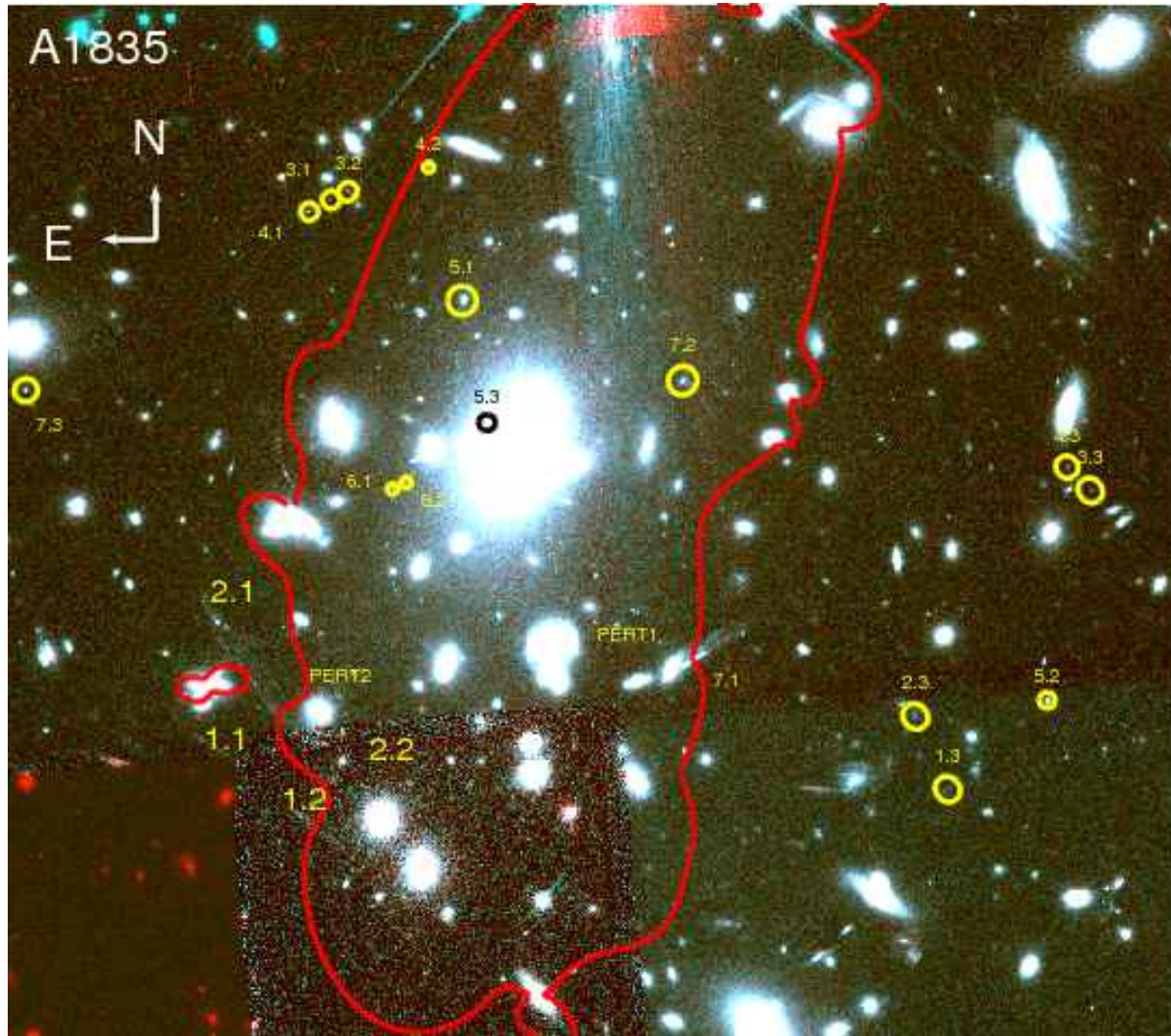


Fig. 2

Continued. The critical lines are presented at redshift 2.07 (A 1835, system 7), 2.0 and 2.7 (A 1413), 2.1 (RXJ1720) and 2.0 (RXJ2129).

The mass models generally include a single dPIE component centred at the BCG location, but in some cases this description is unable to reproduce the observed multiple-image systems. When this is the case, we add a second or third cluster-scale mass component. A full discussion of our capacity to identify cluster-scale clumps from the strong lensing signal is provided in §3.4.3.

In order to estimate the model dependence of our strong lensing results, we also independently fit the cluster-scale mass distributions with the same number of Navarro-Frenk-White (Navarro et al. 1997, hereafter NFW) profiles, characterized by a concentration  $c_{200}$  and a scale radius  $r_s$ , described by usual density profile:

$$\rho(r) = \frac{\rho_c \delta_c}{(r/r_s) (1 + (r/r_s))^2} \quad (2)$$

where  $\rho_c$  is the critical density and  $\delta_c$  is related to  $c_{200}$  through the relation:

$$\delta_c = \frac{200}{3} \frac{c_{200}^3}{\ln(1 + c_{200}) - c_{200}/(1 + c_{200})}. \quad (3)$$

The generalisation of this spherical model into a projected elliptical mass distribution follows a similar relation as Eq. 1. The full analytical description of the pseudo-elliptical NFW is presented in Golse & Kneib (2002).

### 3.2.2 Galaxy-scale mass component

The presence of numerous cluster galaxies near the cluster centre, as identified by our near-infrared photometric selection (§2.2.3) affects the shape of the mass distribution locally, and therefore the associated lensing signal. Following Kneib et al. (1996) and Sm05, we account for galaxy-scale mass in the models by adding individual dPIE mass components at the location of each galaxy in the cluster catalogs discussed in §2.2.3, within 250kpc of the respective BCGs. The geometrical parameters of these components ( $x_c, y_c, e, \theta$ ) are matched to the values measured by SExtractor. The parameters  $\sigma_0, r_{\text{core}}$  and  $r_{\text{cut}}$ , upon which the total mass of each galaxy-scale dark matter halo depend, are assumed to scale with their  $K$ -band luminosity  $L_K$ , relative to an  $L_K^*$  galaxy, following the Faber & Jackson (1976) relation and a constant mass-to-light ratio:

$$\begin{aligned} r_{\text{core}} &= r_{\text{core}}^* (L_K/L_K^*)^{1/2}, \\ r_{\text{cut}} &= r_{\text{cut}}^* (L_K/L_K^*)^{1/2}, \\ \sigma_0 &= \sigma_0^* (L_K/L_K^*)^{1/4} \end{aligned} \quad (4)$$

Similar scaling relations have been used in the past (Covone et al. 2006; Limousin et al. 2007b; Elíasdóttir et al. 2007), showing that  $r_{\text{core}}^*$  is small and has little effect on the modelling results. We therefore adopt  $r_{\text{core}}^* = 0.15\text{kpc}$ , following Limousin et al. (2007b); see also Brainerd & Specian (2003).

The two remaining parameters ( $\sigma_0^*, r_{\text{cut}}^*$ ) are degenerate, because the perturbation of the cluster lensing signal caused by an individual galaxy depends on the total galaxy mass, given by  $\sigma_0^2 r_{\text{cut}}$ . After performing various tests with Lenstool, we concluded that fixing one of these parameters does not affect the ability of the models to reproduce the observed multiple-image systems, provided that

galaxies located within  $2''$  of a highly magnified arc are excluded from the scaling relations (see §3.2.3). We therefore adopted a fixed  $r_{\text{cut}}^* = 45\text{kpc}$ , which matches recent galaxy-galaxy weak-lensing results Natarajan et al. (2009). For our adopted value of  $r_{\text{core}}^* = 0.15\text{kpc}$  the measured galaxy velocity dispersions ( $\sigma$ ) and dPIE velocity dispersions ( $\sigma_0$ ) are in good agreement  $-0.94 < \sigma/\sigma_0 < 1.04$  – the range of values arising from the range of radii at which  $\sigma$  is measured (Elíasdóttir et al. 2007). We therefore employ a Gaussian prior of  $\sigma_0^* = (158 \pm 27)\text{km s}^{-1}$ , making use of Bernardi et al. (2003)’s observational results on  $\sigma^*$ .

### 3.2.3 BCG and individual galaxy perturbers

We model separately the brightest cluster galaxy (BCG) in each cluster using a similar dPIE profile as other cluster members, but optimizing the values of  $\sigma_{0,\text{BCG}}$  and  $r_{\text{cut},\text{BCG}}$  independently. The same approach was used for 6 local galaxy-scale perturbers in A 611, A 773, A 1413, A 1835, identified in Fig. 2.

### 3.2.4 Optimization

The models are fitted to the multiple-image constraints using the new Bayesian Markov chain Monte-Carlo (hereafter MCMC) sampler, described in detail in Jullo et al. (2007). This process uses the observational constraints (positions of the multiply imaged systems) to optimize the parameters describing the mass distribution by matching the location of each image of a given system in the source plane. The quality of the models can be estimated using the root mean square (RMS) deviation in the image-plane from the observed positions of the multiple-image positions predicted by the model, defined as:

$$\sigma_i = \sqrt{\sum_{j,k} (\text{xobs}_{j,k} - \text{xpred}_{j,k})^2 + (\text{yobs}_{j,k} - \text{ypred}_{j,k})^2} \quad (5)$$

where  $(\text{xobs}_{j,k}, \text{yobs}_{j,k})$  and  $(\text{xpred}_{j,k}, \text{ypred}_{j,k})$  are the observed and predicted locations of image  $j$  in system  $k$ , respectively. Following Sm05, Limousin et al. (2007b); Richard et al. (2009) we have used  $0.2''$  as the positional uncertainty of the multiple image identifications.

## 3.3 Best fit parameters

The best fit parameters of the mass models are listed in Table 6, for both models that parameterize the cluster-scale mass components as dPIE and NFW profiles. The parameter uncertainties are based on the MCMC chains generated by Lenstool (see Jullo et al. 2007, for details). We obtain  $\sigma_i \lesssim 0.5''$  for 9/10 clusters, with 7/10 having  $\sigma_i \lesssim 0.2''$ . These results are typical of strong lensing studies using a similar number of multiples images (Richard et al. 2007; Limousin et al. 2007b; Richard et al. 2009). However in the case of A 1835, where we have the largest number of multiple-image constraints (7 systems), we obtained  $\sigma_i \sim 3.15''$ , which is comparable with recent results on A 1689 ( $2.87''$ , Limousin et al. 2007b) using 32 systems. We discuss the origin of this large value of  $\sigma_i$  for A 1835 in §3.4.1.

The best fit ellipticity  $e$  and position angle  $\theta$  of the

**Table 6.** Best-fit parameters of the mass models. For each mass component, we give the centre, ellipticity, orientation, core and cut radii, as well as central velocity dispersion of the dPIE profile. The following column gives the image plane RMS of this model, and the 2 rightmost columns present the best-fit concentration and scale radius of the corresponding NFW profile, used to derive the systematic errors on the model.

Comp.	$\Delta\alpha$ [ $''$ ]	$\Delta\delta$ [ $''$ ]	$e$	$\theta$ [deg]	$r_{\text{core}}$ [kpc]	$r_{\text{cut}}$ [kpc]	$\sigma_0$ [km s $^{-1}$ ]	rms [ $''$ ]	$c_{\text{NFW}}$	$r_{s,\text{NFW}}$ [kpc]	rmsNFW [ $''$ ]
<hr/>											
A521											
DM1	[0.0]	[0.0]	0.67±0.03	49.5±0.7	18.5±3.2	[1000.0]	553±23	0.23	10.4±3.2	64.4±44.8	0.14
BCG	[0.0]	[0.0]	[0.238]	[47.6]	[0.0]	14.1±15.2	20±71				
L* gal					[0.15]	[45]	124±12				
<hr/>											
A611											
DM1	[0.0]	[0.0]	0.37±0.01	-47.3±0.4	42.3±2.8	[1000.0]	854±9	0.21	8.7±0.4	161.7±11.1	0.30
PERT1	[-10.8]	[10.3]	[0.346]	[88.10]	[0.109]	[32.60]	133±8				
BCG	[0.0]	[0.0]	[0.346]	[-61.5]	[0.0]	99.6±26.5	304±32				
L* gal					[0.15]	[45]	124±5				
<hr/>											
A773											
DM1	[0.0]	[0.0]	0.62±0.15	-37.3±6.3	42.1±27.5	[1000.0]	501±79	0.45	6.1±1.9	187.8±43.4	0.34
DM2	[0.0]	[24.0]	0.47±0.08	-20.2±7.7	128.2±20.3	[1000.0]	836±99		4.1±1.0	267.4±86.1	
DM3	-119±11	6±7	0.42±0.17	-54.4±54.8	[75.0]	[1000.0]	996±94		9.2±2.1	196.2±148.3	
BCG	[0.0]	[0.0]	[0.297]	[-41.0]	[0.396]	[79.272]	353±103				
PERT1	[-0.6]	[24.0]	[0.208]	[10.0]	[0.421]	[84.163]	411±111				
PERT2	[-52.2]	[7.5]	[0.373]	[-43.80]	[0.138]	[41.42]	169±13				
L* gal					[0.15]	[45]	177±10				
<hr/>											
A868											
DM1	[0.0]	[0.0]	[0.0]	[-66.5]	71.4±26.4	[1000.0]	1078±257	0.05	7.9±3.5	33.4±193.1	0.04
DM2	[-21.5]	[11.7]	0.42±0.12	26.2±17.0	62.8±18.3	[1000.0]	426±93		2.3±2.6	748.7±209.5	
L* gal					[0.15]	[45]	161±26				
<hr/>											
Z2701											
DM1	[0.0]	[0.0]	0.28±0.05	55.4±1.9	64.6±16.5	[1000.0]	1008±70	0.11	3.3±1.2	711.8±151.5	0.19
BCG	[0.0]	[0.0]	[0.18]	[60.9]	[0.0]	9.3±27.7	292±55				
L* gal					[0.15]	[45]	79±26				
<hr/>											
A1413											
DM1	[0.0]	[0.0]	0.67±0.02	85.1±0.5	67.1±5.9	[1000.0]	941±23	0.53	2.9±0.5	691.4±108.8	0.57
BCG	[0.0]	[0.0]	[0.710]	[65.0]	[0.06]	125.7±35.9	334±16				
PERT1	[13.2]	[-19.9]	[0.116]	[36.60]	[0.104]	[31.247]	168±8				
L* gal					[0.15]	[45]	107±4				
<hr/>											
A1835											
DM1	4.8±0.0	0.7±0.3	0.57±0.01	77.7±0.1	99.1±1.3	[1000.0]	1219±2	3.15	5.7±0.1	341.0±8.3	2.96
BCG	1.4±0.1	-0.3±0.1	[0.142]	[70.0]	[4.384]	24.7±1.5	880±13				
PERT1	[15.0]	[-19.8]	[0.720]	[60.6]	[0.098]	94.1±34.6	111±30				
PERT2	[-17.6]	[-23.7]	[0.229]	[-36.7]	[0.124]	2.5±3.5	363±43				
L* gal					[0.15]	[45]	[158]				
<hr/>											
A2204											
DM1	[0.0]	[0.0]	0.54±0.15	134.6±5.3	13.2±18.5	[1000.0]	556±158	0.29	3.5±3.2	687.5±197.8	0.20
L* gal					[0.15]	[45]	238±25				
<hr/>											
RXJ1720											
DM1	[0.0]	[0.0]	0.59±0.19	[-66.9]	9.9±17.3	[1000.0]	539±143	0.15	13.9±3.2	61.4±168.8	0.24
L* gal					[0.15]	[45]	127±22				
<hr/>											
RXJ2129											
DM1	[0.0]	[0.0]	0.46±0.15	-16.4±2.5	45.2±13.9	[1000.0]	755±98	0.11	5.9±2.0	198.6±79.8	0.23
BCG	[0.0]	[0.0]	[0.490]	[-35.4]	[0.172]	[1.988]	335±129				
L* gal					[0.15]	[45]	229±35				

cluster-scale dark matter halos are in good agreement between the dPIE and NFW models, with  $0 \lesssim e \lesssim 0.7$ , and  $\theta$  of the main cluster-scale halo agreeing with the orientation of the BCG. A few clusters have  $e > 0.5$ ; Golse & Kneib (2002) have shown that the pseudo-elliptical NFW profile presents a boxy/peanut shape at such high ellipticities. We

therefore adopt the dPIE models as the fiducial models for the rest of the paper, and use the NFW models to quantify systematic errors in §3.4.

For 8/10 clusters a single dPIE or NFW cluster-scale dark matter halo is needed in addition to the cluster galaxies to reproduce accurately the observed multiply-imaged

systems. However, for two clusters, the strong lensing constraints reveal the influence of additional cluster-scale dark matter halos:

- A 868: The overall shape of the giant arc providing the constraints in this cluster is quite straight, and slightly curved towards the second brightest galaxy instead of the cluster centre. This shows that it is mostly influenced by the presence of a secondary component, which we parametrize as centred on this second galaxy.
- A 773: The large number of highly sheared arcs and multiple images show the presence of a dual component at the centre, as well as a third dark matter clump towards the east. Using the new spectroscopic redshifts of multiple images, we confirm the result of Sm05, who included 3 components in the lens model to explain the overall weak-lensing signal.

We compare the magnification factors  $\mu$  computed from the lens models with the photometry of each image in a given multiple system (last columns of Table 4). We find only a marginal agreement between the measured photometry and these magnifications, which is certainly due to the fact that the magnification factors are derived only at a single position, whereas many of the arcs are fairly extended, and also due to the surface brightness limits when measuring the photometry of the faintest images. The majority of the multiple images are strongly magnified, with typically  $\mu \sim 2$  mags (or 5 – 10 on linear scale). Errors on the magnification reach very large values ( $\Delta\mu > 1$  mag) for multiple images in the vicinity of the critical line ( $\mu \gtrsim 4$  mags, or  $\gtrsim 30$  on linear scale).

### 3.4 Systematic Errors

In this section we discuss four systematic uncertainties in our mass models: inability of parameterized models to fit the multiple-image constraints in A 1835 (§3.4.1), the impact of fixing the size of  $L^*$  galaxies on the modeling results (§3.4.2), reliability of identification of substructures (§3.4.3), and choice of parameterization for cluster-scale dark matter halos (§3.4.4).

#### 3.4.1 Quality of Fit for A 1835

We tried to improve the quality of the fit to the multiple-image constraints in A 1835 ( $\sigma_i \simeq 3''$ ) by adding a secondary dPIE cluster-scale halo on the next brightest peaks seen on the  $K$ -band light map (see §3.4.3), as well as allowing the positions of the main cluster-scale halo (previously with its centre fixed on that of the BCG) to be free parameters. This did not yield any significant improvements in the quality of the fit. The high value of  $\sigma_i$  is due to the inability of the parameterized model to reproduce simultaneously the multiple-image systems located to the North and to the South of the BCG. It therefore appears that the main limitation of the current model for this cluster is the assumption of elliptical symmetry in the mass components.

To explore this, we used the new, more flexible method presented by Jullo & Kneib (2009) that employs a multi-scale adaptive grid to refine a parametric model that is constrained by a large number of strong lensing constraints –

thus dropping the assumption of elliptical symmetry. The resulting mass map shows a mass extension to the North of the BCG and less extended to the South, compared to the original dPIE model. The quality of the fit is improved to  $\sigma_i = 1.7''$  for the same multiply-imaged systems. The lack of spectroscopic redshifts in the Northern multiple images precludes strong conclusions about this asymmetry. Securing spectroscopic redshifts for these multiple-image systems is therefore a necessary step to further improve this mass model. Overall, the absence of a secondary cluster-scale component in the simple dPIE model and the wide distribution of multiply-imaged galaxies across the cluster core reassure us that the absolute calibration of the total mass, Einstein radius and cluster substructure are reasonably accurate.

#### 3.4.2 Fixed Size of $L^*$ Cluster Galaxies

We note that other galaxy-galaxy weak-lensing works have obtained different values for  $r_{\text{cut}}^*$ , but within the range  $10 < r_{\text{cut}}^* < 100$  kpc (Natarajan et al. 2002; Limousin et al. 2007a; Halkola et al. 2007). To quantify how much our choice of  $r_{\text{cut}}^* = 45$  kpc (§3.2.2) affects mass model results, we therefore ran the following test: we included  $r_{\text{cut}}^*$  as a free parameter for the 5 models having the largest number of constraints (i.e. A 611, A 773, A 1413, A 1835 and Z 2701), allowing it to vary in the range  $[10 - 100]$  kpc. The best fit parameters and quality of fit (judged by  $\sigma_i$ ) of these 5 models are all consistent with the fiducial models in Table 6, specifically, the best-fit values of  $r_{\text{cut}}^*$  are all consistent with  $r_{\text{cut}}^* = 45$  kpc within their respective statistical uncertainties. The degeneracy between  $r_{\text{cut}}^*$  and  $\sigma^*$  also obey the expected  $r_{\text{cut}}^* \sigma^{*2} = \text{Const.}$  relation – i.e. a constant amount of mass is assigned to galaxy-size haloes (within 10%) regardless of the specific values of these two parameters. This folds through to an uncertainty of just 15% on the cluster substructure fractions, which is negligible in comparison with the statistical errors.

#### 3.4.3 Identification of Massive Substructures

The necessity or not to add a second or third cluster-scale mass component to reproduce the observed multiple-image systems has been determined by the number and location of the strong-lensing constraints. The presence of massive substructures has direct implications on the substructure measurements discussed in §4. We therefore test the fiducial mass models by comparing quantitatively the distribution of  $K$ -band light in the cluster cores with the mass modeling results.

We constructed  $K$ -band luminosity density maps from the cluster galaxy catalogues discussed in §2.2.3, with a Gaussian smoothing scale of  $\text{FWHM} = 20''$  (corresponding to  $\sim 70$  kpc at  $z = 0.2$ ), which is the smallest scale over which we measured the influence of a secondary clump on the strong lensing images. The location of the highest peak ( $L_{K,\text{max}}$ ) in the  $K$ -band light maps always coincides (within  $1''$ ) with the centre of the cluster-scale mass distribution. We searched for secondary peaks in the  $K$ -band light by adopting a threshold  $L > 0.5L_{K,\text{max}}$  and look for the local maxima within these regions (Figure 3, white crosses). When comparing their location with the cluster-scale dark

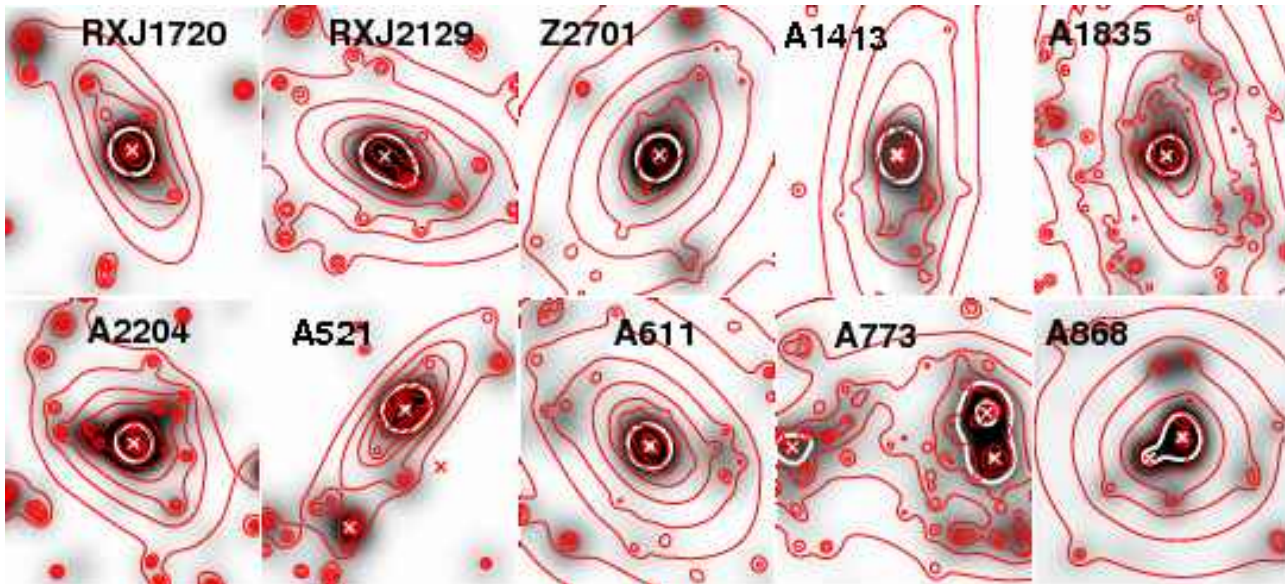


**Figure 3.** *K*-band cluster luminosity density maps (gray scale) smoothed with a FWHM=20'' gaussian. Red contours show the reconstructed dark matter distribution with a constant logarithmic scale. The white contours show the selection of *K*-band light peaks as local maxima (crosses, see §3.4.3 for details).

matter clumps, we find that every local maximum is coincident with a cluster-scale mass component in our models within the modelling errors (1''), except for the secondary peak in A 521 (located  $\sim 1'$  South of the BCG). It therefore appears that we are unable to detect this structure because the strong-lensing constraints lie exclusively North of the BCG. The presence of substructure in A 521 is consistent with the dynamical study of Maurogordato et al. (2000), who identified many large-scale components in A 521, and suggested that it is a highly disturbed merging cluster. Our inability to detect any of these structures may explain why A 521 is an outlier in the  $f_{\text{sub}} - \Delta m_{12}$  relation discussed in §4.2.2.

#### 3.4.4 Parameterization of Dark Halos

To examine the amplitude of any systematic error in cluster mass measurement arising from choice of dPIE or NFW mass profiles, we show the projected mass profiles  $M_{\text{SL}}(R)$  in Fig. 4 from both dPIE and NFW models. The statistical error on  $M_{\text{SL}}(R)$  is typically 0.05 to 0.2dex, depending on the number of lensing constraints. We find a general agreement between the  $M_{\text{SL}}(R)$  profiles obtained from the best-fitting dPIE and NFW models, and use the average difference between the two as an estimate of the systematic error made by assuming a specific cluster-scale profile – this systematic error is comparable with the statistical errors.

## 4 THE MASS AND STRUCTURE OF CLUSTER CORES

In this section we use the strong lens models of the full sample of 20 clusters to construct a statistical sample of measurements of the mass and structure of cluster cores, for comparison with theoretical predictions. Despite the modest statistical significance achieved in these comparisons, due to

the sample size, this is so far the largest sample of strong lensing clusters analyzed in a uniform manner, and represents a four-fold increase on the strong-lensing clusters studied by Sm05. Most importantly, these results provide a statistical context within which to view results from detailed analysis of spectacular individual cluster lenses.

We begin by describing integrated cluster masses and related quantities such as Einstein radii in §4.1, and then concentrate on structural quantities such as substructure fractions and cluster ellipticities in §4.2.

### 4.1 Cluster Masses and Einstein Radii

#### 4.1.1 Einstein radii

We first measure the effective Einstein radius  $\theta_E$  of each cluster at  $z_s = 2$ .  $\theta_E$  is defined as the angular radius  $\theta$  from the centre of the cluster at which the average convergence  $\bar{\kappa}(\theta < \theta_E) = 1$  (Broadhurst & Barkana 2008). We choose  $z_s = 2$  because this is the typical redshift of the spectroscopically confirmed multiply-imaged galaxies (Table 4). Values of  $\theta_E$  range between  $\sim 4''$  and  $47''$ , are listed in Table 7, and the distribution is plotted in Fig. 5. The  $\theta_E$  distribution is best-fitted by a log-normal distribution with  $\langle \log_{10} \theta_E \rangle = 1.16 \pm 0.28$ , where  $\theta_E$  is measured in arcseconds. Two clusters (A 1689 and Abell 1703) are in common between this study and the Broadhurst & Barkana (2008) sample of clusters with large Einstein radii. These two clusters are located at  $2\sigma$  and  $1.5\sigma$  above  $\langle \log_{10} \theta_E \rangle$ , suggesting that  $\sim 2.3\%$  and  $\sim 6.7\%$  of clusters found in larger sample will have  $\theta_E$  at least as large as those of A 1689 and A 1703 respectively.

Comparison of observed Einstein radii with theoretical predictions from numerical simulations is problematic because the simulations require both sufficiently large volume to contain a large sample of clusters as massive as observed systems, and sufficient numerical resolution to allow  $\theta_E$  to

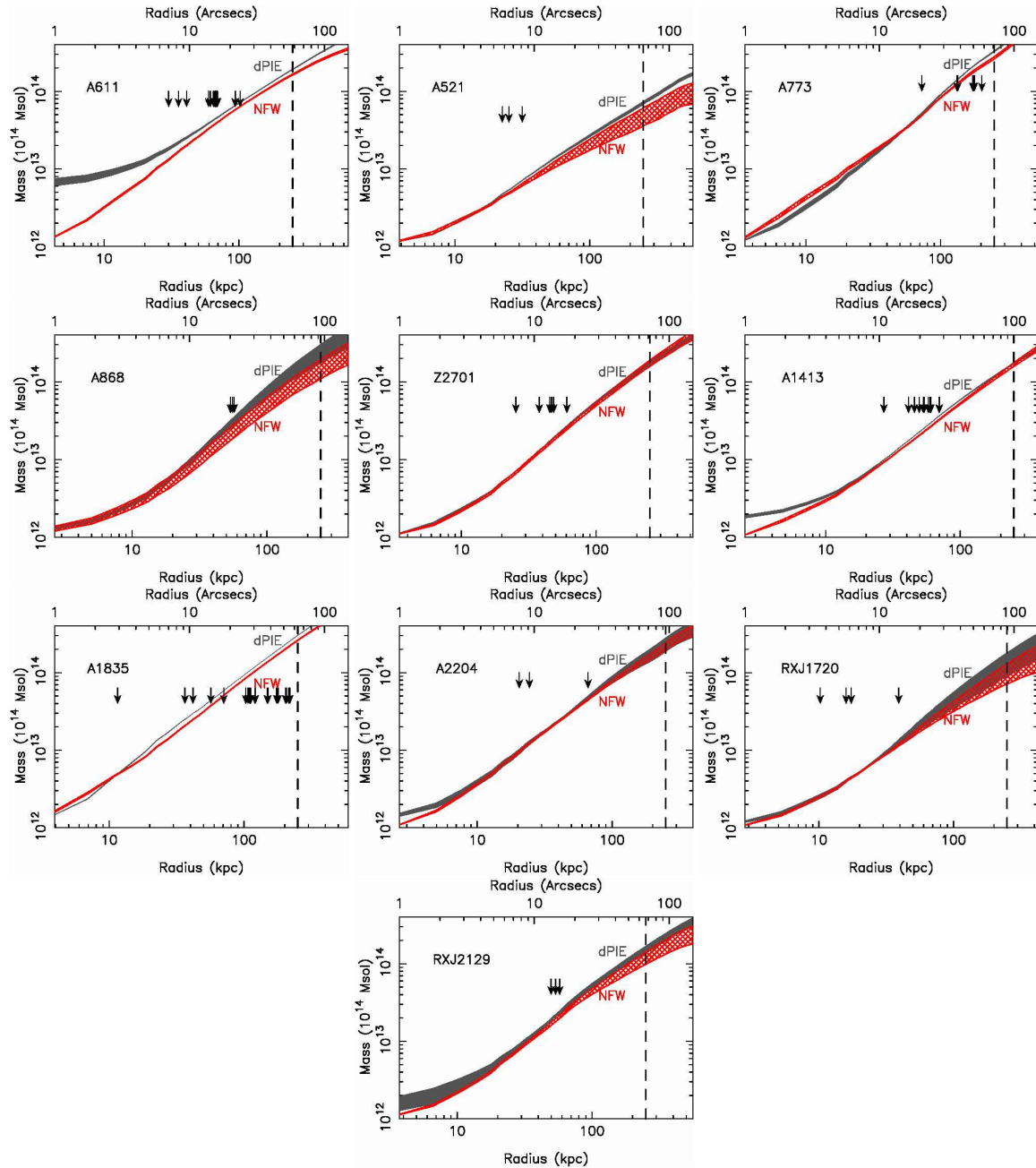


**Figure 4.** Integrated mass profiles assuming a dPIE (solid grey) or a NFW (hatched red) profile for the dark-matter distribution. The arrows mark the distance of the multiple images used as constraints in each cluster, and the vertical dashed corresponds to the radius of 250kpc used to derive the enclosed masses.

be measured reliably from the simulated data. Even modern simulations such as the Millennium Simulation are unable to satisfy both requirements, the main shortcoming being the simulation volume. Nevertheless, it is interesting to make a comparison. We therefore take the best-fit mass and concentration of the ten NFW models in Table 6 and convolve the measured concentrations with the predicted concentration distributions in Broadhurst & Barkana (2008). We then calculate the predicted  $\theta_E$  distributions and sum them to produce the red dashed curve in Fig. 5. This distribution is much broader than the observed distribution, mainly because the virial masses of the NFW models are

poorly constrained by strong-lensing constraints alone. In spite of this, we find that the predicted distribution peaks at  $\theta_E \approx 5''$ , a factor of 2 lower than the observed distribution. This difference may be caused by an important difference between the simulations and observations, namely the presence of baryons in observed universe and the absence of them from the simulations. However it is interesting to note that in a recent weak-lensing study of similarly sized sample, Okabe et al. (2009) found that the normalization of the mass-concentration of observed clusters is roughly a factor of 2 higher than predicted from numerical simulations. The



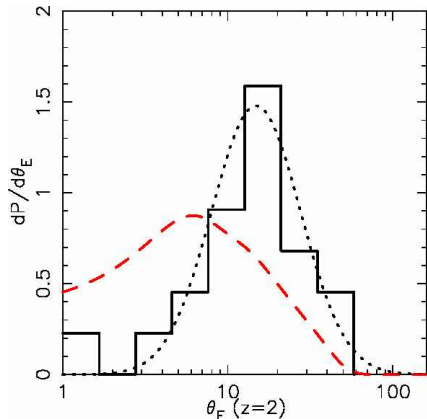


**Figure 5.** The observed distribution of effective Einstein radii for a source at  $z_s = 2.0$  (solid black histogram), and best-fit lognormal distribution (black dotted line). We also plot the predicted distribution based on the NFW model parameters (Table 6), and the predicted distributions of halo properties in strong-lensing selected simulated clusters – see §4.1.1 for more details.

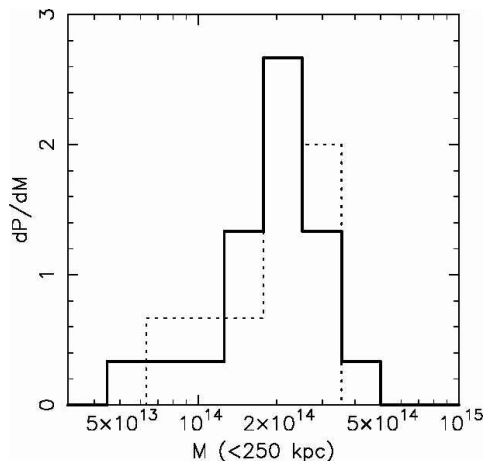


**Figure 6.** Probability distribution of lensing masses (measured in a projected radius of 250 kpc) for the Sm05 sample (dashed histogram) and the current sample (solid histogram).

physical origin of both differences, if confirmed by larger samples, may be similar.

#### 4.1.2 Projected Mass Measurements

We show projected mass maps of the 10 new strong-lensing clusters in Fig. 3, and integrate these maps and their equivalents for the extended sample to measure the projected mass of the cluster cores  $M_{\text{SL}}(R < 250\text{kpc})$  – see Table 7. The mass measurements for the extended sample were based on the published dPIE models of these clusters listed in Tables 2 & B1, adjusted to the cosmology used in this paper where relevant. The aperture of  $R < 250\text{kpc}$  is chosen because this ensures that the region within we measure mass lies within the *HST* field of view for all clusters; it is also  $\sim 2\times$  the largest observed Einstein radius within this sample.

We compare the  $M_{\text{SL}}(R < 250\text{kpc})$  distribution of the current sample with the 10 clusters studied by Sm05 in Fig. 6, and fit a log-normal distribution to both samples, obtaining:

$\langle \log_{10}(M_{\text{SL}}) \rangle = 14.29 \pm 0.19$  and  $14.27 \pm 0.17$  for our sample and Sm05 respectively. This confirms that both studies are probing clusters of the same mass, which is consistent with close match in the range of X-ray luminosity probed:  $4.3 \times 10^{44} \leq L_X \leq 22.8 \times 10^{44} \text{erg s}^{-1}$  in the case of Sm05, and  $3.5 \times 10^{44} \leq L_X \leq 22.8 \times 10^{44} \text{erg s}^{-1}$  here (Table 7).

We also plot in Fig. 7 the relationship between  $\theta_E$  and  $M(< 250\text{kpc})$ , revealing a clear positive linear correlation between the two quantities, as is expected from the properties of analytic descriptions of dark matter density profiles from simulations. The best-fit relation for the whole sample is  $\theta_E = (-14.7 \pm 4.7) + (13.8 \pm 2.5) M_{\text{SL}}$ ; the best-fit relations for cool-core and non-cool core sub-samples are both statistically indistinguishable from this relation. However, we find that disturbed clusters tend to lie below the best-fit relation for the full sample – indeed, we obtain best-fit relations of:  $\theta_E = (-8.6 \pm 4.5) + (9.75 \pm 2.3) M_{\text{SL}}$  and  $\theta_E = (-14.7 \pm 5.0) + (14.0 \pm 2.2) M_{\text{SL}}$  for disturbed and undisturbed clusters, respectively. We interpret this as implying that disturbed clusters have flatter density profiles than undisturbed clusters of comparable mass. This is likely due to a combination of (i) the cluster-cluster mergers that are likely to both soften the density profile, and also to cause the observed disturbance (i.e. cause the offset between the X-ray and optical centers of the clusters), and (ii) disturbed clusters tending to have their merger axis preferentially aligned in the plane of the sky, thus making the disturbance possible to measure. This latter point is of particular importance with respect to A 1689, because this cluster is classified as undisturbed despite there being strong evidence for it being a line-of-sight merger (Limousin et al. 2007b). If this cluster were viewed side-on, then it would probably lie below the relation for undisturbed clusters, and be classified as disturbed.

#### 4.1.3 Comparison of Lensing and X-ray Mass Measurements

We further investigate the integrated mass of the cluster cores within  $R < 250\text{kpc}$  by comparing the  $M_{\text{SL}}$  with masses measured within the same aperture from the X-ray models discussed in §2.4. We used least-squared minimization, taking account of errors in both quantities to find the best fit parameters of the relation:  $M_{\text{SL}} = B M_X$ . For the full sample, we obtain a best-fit of  $\log_{10}(B) = 0.13 \pm 0.04$ , i.e. a mean X-ray/lensing mass discrepancy of a factor of  $M_{\text{SL}}/M_X = 1.3$  at  $\sim 3\sigma$  significance.

We then fit the same relations for the cool core/non-cool core as well as disturbed/undisturbed cluster subsamples, and report the best fit values in Table 8. We find that the disturbed/undisturbed sub-samples are statistically indistinguishable from both each other and from the entire sample. However, we find that the normalization,  $\log_{10}(B)$ , of the relation for non-cool-core clusters is  $2\sigma$  higher than for cool-core clusters. These differences are illustrated in Fig. 8.

To test the link between the agreement between lensing and X-ray mass measurements and the mass estimates and the structure of the cluster cores in more detail, we plot  $M_{\text{SL}}/M_X$  against  $\alpha$ ,  $f_{\text{sub}}$  (§4.2.1) and X-ray/BCG offset in Fig. 9. There is considerable scatter in all three panels, however we try to fit a straight-line relation to the data in each case. We obtain a positive correlation be-

**Table 7.** The mass and structure of the cluster cores inferred from the strong-lensing mass models, plus related quantities from the near-infrared cluster galaxy catalogs.

Cluster	$N_{\text{mult}}^a$	Radial? <sup>b</sup>	$M_{\text{SL}}^c$	$e_{2\text{D}}^d$	$\theta_E (z=2)$ (arcsec)	$f_{\text{sub}}$	$L_{\text{K,BCG}}/L_{\text{K,tot}}$	$\Delta m_{12}$ (mags)
A 521	1	No	0.61±0.33	0.66	3.6 ± 0.8	0.13 ± 0.04	0.22 ± 0.03	0.05
A 611	4	Yes	1.76±0.33	0.36	21.0 ± 1.3	0.10 ± 0.01	0.44 ± 0.06	2.16
A 773	3	Yes	3.01±0.58	0.385	30.1 ± 1.2	0.78 ± 0.03	0.13 ± 0.02	0.13
A 868	1	No	1.97±1.11	0.06	14.2 ± 5.6	0.26 ± 0.12	0.25 ± 0.04	0.81
Z2701	2	No	1.74±0.14	0.34	9.0 ± 0.5	0.04 ± 0.02	0.45 ± 0.06	2.33
A 1413	4	No	1.71±0.20	0.64	11.9 ± 0.5	0.07 ± 0.01	0.32 ± 0.05	1.80
A 1835	7	Yes	2.83±0.41	0.49	30.5 ± 0.5	0.13 ± 0.01	0.26 ± 0.09	1.57
A 2204	1	Yes	2.29±0.50	0.27	23.9 ± 2.2	0.25 ± 0.10	0.13 ± 0.02	0.14
RXJ1720	1	Yes	1.18±0.59	0.59	7.0 ± 0.5	0.10 ± 0.05	0.47 ± 0.07	1.60
RXJ2129	1	No	1.37±0.37	0.56	9.0 ± 1.4	0.15 ± 0.06	0.40 ± 0.06	1.26
Extended sample – see Table 2 for mass model references								
A68	6	No	2.16±0.23	0.23	7.5±0.5	0.33±0.04	0.32±0.04	1.40
A383	3	Yes	1.87±0.26	0.22	10.4±2.6	0.02±0.01	0.46±0.06	1.90
A963	2	No	1.74±0.44	0.355	7.5±0.5	0.13±0.07	0.38±0.05	1.26
A1201	1	No	0.80±0.33	0.66	1.5±0.15	0.02±0.01	0.64±0.09	2.54
A2218	6	Yes	3.00±0.24	0.23	18.3±0.5	0.54±0.01	0.18±0.03	0.46
A2219	6	Yes	2.33±0.23	0.41	15.6±0.6	0.57± 0.04	0.22±0.03	0.75
A2390	4	No	1.99±0.07	0.14	17.5±0.5	0.03±0.03	0.30±0.04	1.53
A2667	3	No	2.41±0.07	0.39	13.0±0.6	0.14±0.03	0.17±0.02	0.87
A1689	34	Yes	4.53±0.13	0.22	47.1±0.5	0.22±0.03	0.24±0.02	0.68
A1703	16	Yes	2.98±0.09	0.39	36.8±1.5	0.15±0.02	0.52±0.07	1.57

<sup>a</sup> Number of strongly-lensed galaxies used to constrain the mass model. <sup>b</sup> Whether the strong-lensing constraints include a radial image pair. <sup>c</sup> Projected mass within  $R < 250\text{kpc}$  in units of  $10^{14} M_{\odot}$ . <sup>d</sup> Ellipticity of mass distribution in the cluster core inferred from the projected mass maps.**Table 8.** Best fit parameters for the relationship between  $M_{\text{SL}}(R < 250\text{kpc})$  and  $M_X(R < 250\text{kpc})$  discussed in §4.1.3.

Sample	$N_{\text{clus}}^a$	Normalization $\log_{10}(B)$	Scatter $\sigma_M$ (dex)
All <sup>b</sup>	18	0.13 ± 0.04	0.17
Cool core	8	0.05 ± 0.05	0.19
Non cool core	10	0.17 ± 0.04	0.13
Undisturbed	12	0.15 ± 0.05	0.20
Disturbed	6	0.12 ± 0.04	0.15

<sup>a</sup> The number of clusters in each sub-sample are taken from Table 5 <sup>b</sup> Chandra data are not available for two of the clusters – A 868 and A 1703.

tween  $M_{\text{SL}}/M_X$  and all of  $\alpha$ ,  $f_{\text{sub}}$  and offset, as shown by the dashed lines in Fig. 9, however the  $M_{\text{SL}}/M_X$  vs  $f_{\text{sub}}$  is the only one of the three with a slope that is statistically distinguishable from flat, with a best-fit of  $M_{\text{SL}}/M_X = (1.8 \pm 0.3) + (0.63 \pm 0.35)\log_{10}(f_{\text{sub}}) - \text{i.e. a } \sim 2\sigma$  detection of a dependence of  $M_{\text{SL}}/M_X$  on  $f_{\text{sub}}$ .

We interpret this as evidence that the assumption of hydrostatic equilibrium required by the X-ray mass estimates is less reliable in clusters with larger substructure fractions. Specifically, the merging activity signaled by larger substructure fractions may be adding non-hydrostatic pressure support to the ICM through bulk motions of gas in a manner similar to that identified by Rasia et al. (2006) and Nagai et al. (2007) at larger radii in simulations.

## 4.2 Cluster Substructure, BCG Dominance and Ellipticity

### 4.2.1 Substructure Fractions

Following Sm05 and Smith & Taylor (2008), we define the substructure fraction  $f_{\text{sub}}$  as the fraction of the mass within a radius  $R$  that is not contained in the BCG and the cluster-scale dark matter halo centred on the BCG. This allows straightforward calculation of  $f_{\text{sub}}$  from the mass models, and provides an estimate of the fraction of mass that resides in galaxy- and group-scale halos within the parent cluster. We measure  $f_{\text{sub}}$  within the same aperture as for  $M_{\text{SL}}$ , i.e.  $R < 250\text{kpc}$ . At these scales  $f_{\text{sub}}$  is stable to small changes in the aperture choice; this stability extends down to  $R \gtrsim 100\text{kpc}$  in most cases. The measurements of  $f_{\text{sub}}$  are listed in Table 7.

Smith & Taylor (2008) compared the predicted (from Taylor & Babul 2005) and observed (from Sm05)  $f_{\text{sub}}$  distributions, finding a possible excess of clusters with the highest values of  $f_{\text{sub}}$ . They speculated that, if confirmed, these excesses may be due to X-ray selected clusters comprising an excess of cool core and merging clusters with respect a purely mass-selected sample (the synthetic clusters were selected on mass from Taylor & Babul’s model). We return to this distribution in Fig. 10 with our enlarged sample of 20 strong-lensing clusters (Sm05 comprises 5 strong- and 5 weak-lensing constrained cluster cores). As seen in Fig. 10, the observed  $f_{\text{sub}}$  distribution remains noisy with 20 clusters. We repeat the Kolmogorov Smirnov test of Smith & Taylor, and again obtain an inconclusive result, with the null hypothesis that the observed and sythetic samples are drawn

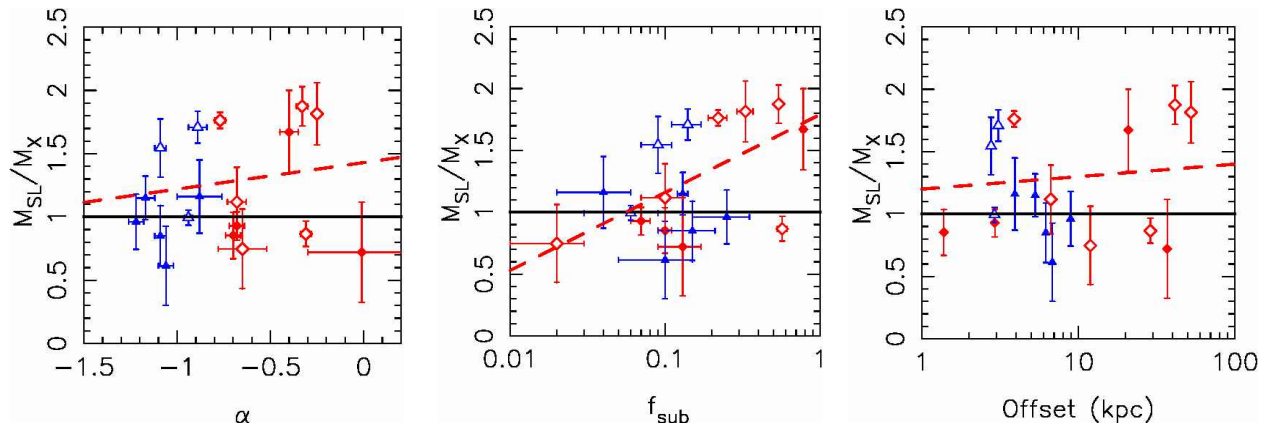


**Figure 9.** Residuals of the  $M_{\text{SL}}/M_X$  relation against the central X-ray slope  $\alpha$  (left panel), the strong-lensing derived substructure fraction (middle panel) or the offset between the X-ray centre and the BCG (right panel). The red dashed line shows the best fitting linear relation for each diagram. Symbols are identical to Fig. 8.

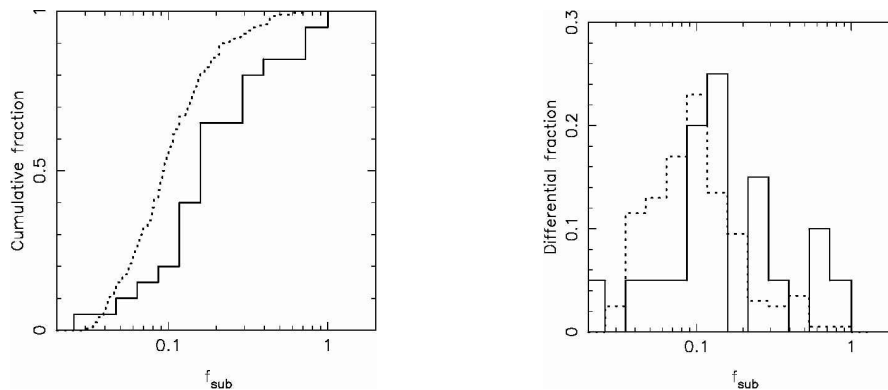


**Figure 10.** Observed substructure fraction (solid curve), as determined from the 20 strong-lensing models in the extended sample, compared with the expected distribution (dashed curve) presented in Smith & Taylor (2008). Left diagram: cumulative distribution. Right diagram: differential distribution.

from the same underlying distribution disfavoured at 80% (i.e.  $1.3\sigma$ ) confidence.

There is extensive discussion in the literature on the issue of whether cluster-cluster mergers are capable of destroying cool cores (e.g. Poole et al. 2008; Burns et al. 2008). We have previously addressed this question indirectly through comparisons of  $\alpha$  and X-ray/BCG offsets in Sanderson et al. (2009a). Here, we tackle it more directly, by comparing  $\alpha$  with  $f_{\text{sub}}$  in Fig. 11. We fit a relation of the form  $\log_{10}(f_{\text{sub}}) = A + B\alpha$  and obtain best fit parameters of  $A=0.09 \pm 0.12$ , and  $B=1.15 \pm 0.22$ . We therefore find a positive correlation at  $5\sigma$  significance between  $f_{\text{sub}}$  and  $\alpha$ , albeit with large scatter. Clusters that host a cool core therefore also have less substructure in their cluster core mass distribution, and vice versa. This supports the connection found in §4.1.3 between the differing values of  $M_{\text{SL}}/M_X$  for cool core and non-cool core clusters, and the positive correlation between the mass ratio and  $f_{\text{sub}}$ . This result is also strongly suggestive that the cluster-cluster merger activity associated with larger values of  $f_{\text{sub}}$  plays a role in destroying cool cores. However the appreciable scatter on this relationship also suggests that the physics is more complicated than a simple one-to-one relationship.

#### 4.2.2 BCG Dominance

The dominance of the BCG over the total  $K$ -band luminosity of cluster galaxies within cluster cores was investigated by Sm05, who found a roughly monotonic relationship between  $L_{K,\text{BCG}}/L_{K,\text{TOT}}$  and  $f_{\text{sub}}$  in the sense that more dominant BCGs live in clusters with lower substructure fractions. This has been investigated in more detail recently by Smith et al. (2009b) who showed that  $\sim 8\%$  of  $10^{15} M_{\odot}$  clusters contain a BCG at least two magnitudes brighter than the second ranked cluster galaxy ( $\Delta m_{12} > 2$ ). We build on these results here by comparing substructure in the total mass distribution in the cluster cores with the dominance of the BCGs for our enlarged sample of 20 strong-lensing clusters. We plot  $f_{\text{sub}}$  versus both the fraction of the cluster  $K$ -band luminosity emanating from the BCG and the magnitude gap between the BCG and the second ranked cluster galaxy in Fig. 12, with both measured within the same  $R < 250\text{kpc}$  region as  $f_{\text{sub}}$ . Both plots show an obvious correlation, confirming and extended the results in Sm05. We obtain best-fit relations of:  $\log_{10}(f_{\text{sub}}) = -2.80 L_{K,\text{BCG}}/L_{K,\text{tot}} + 0.22$  and  $\log_{10}(f_{\text{sub}}) = -0.53\Delta m_{12} - 0.07$ , both relations having a dispersion of  $\sigma \sim 0.3\text{dex}$ .

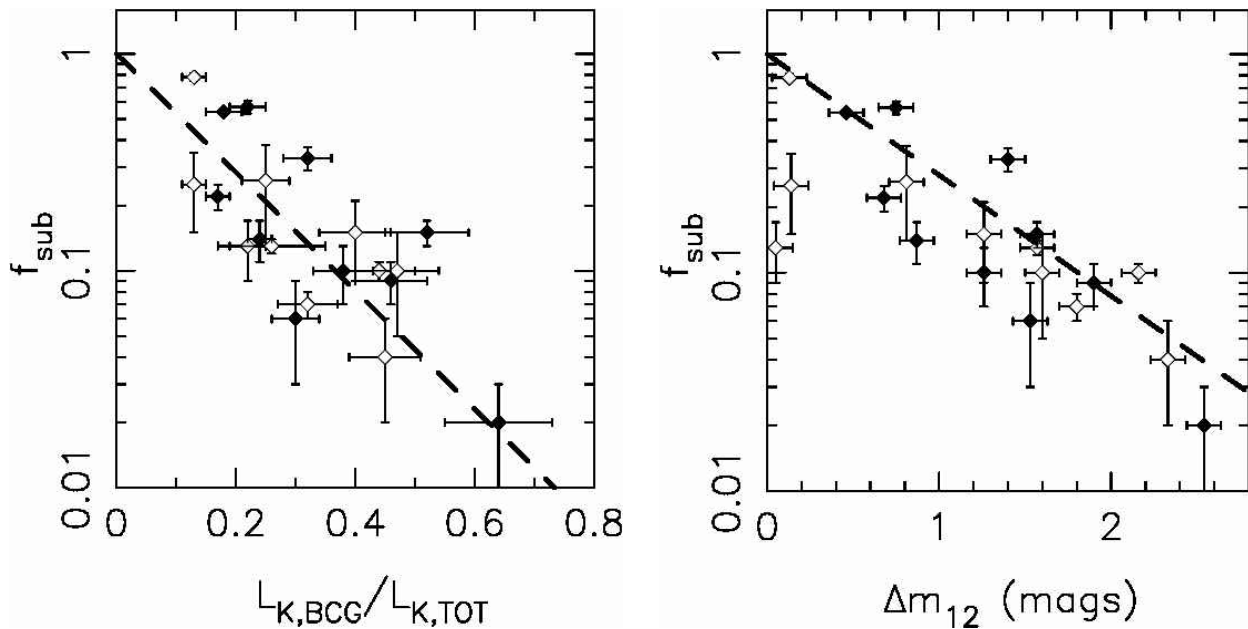


**Figure 12.** Substructure fraction versus indicators of BCG dominance: fraction of the cluster core  $K$ -band luminosity that emanates from the BCG (left) and the magnitude gap between the BCG and the second ranked cluster galaxy (right). Filled symbols are the new clusters, and open symbols are from the extended sample.

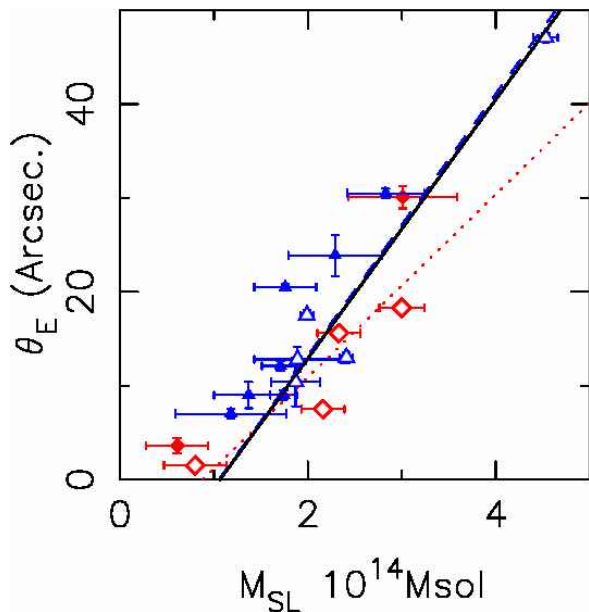


**Figure 7.** Effective Einstein radius (assuming a  $z = 2$  source) vs strong-lensing mass (measured within 250 kpc). The lines show the general trends when least-squared fitting a linear relation for all clusters (black solid line), undisturbed clusters (blue dashed line) and disturbed clusters (red dotted lines). Red diamonds denote disturbed clusters and blue triangles undisturbed clusters. Filled symbols are the new strong lensing models, and open symbols are taken from the extended sample.

#### 4.2.3 Cluster ellipticity

We have measured the 2D ellipticity and orientation of each cluster core mass distribution ( $R < 250$  kpc) by fitting elliptical mass contours with the IRAF routine `ellipse` to the projected mass maps based on the mass models (see

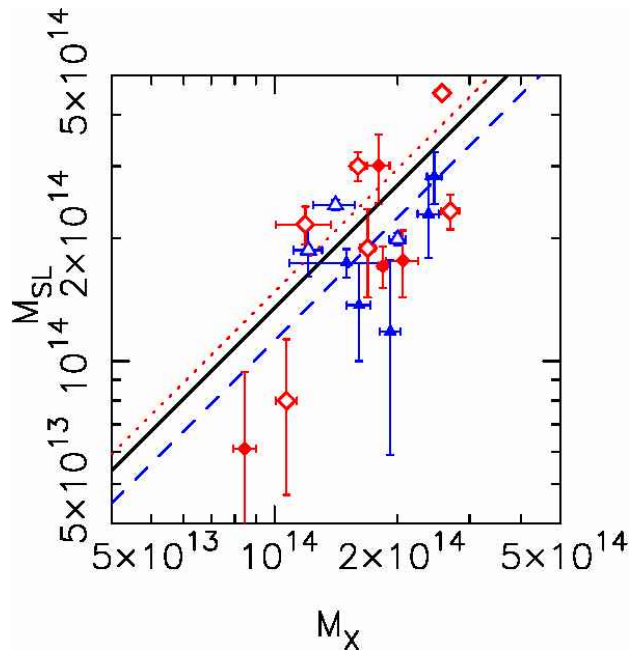


**Figure 8.** Relationship between  $M_X$  and  $M_{SL}$ , both measured within  $R < 250$  kpc. The lines show the general trends when least-squared fitting a linear relation for all clusters (black solid line), cool-core clusters (blue dashed line) and non-cool core clusters (red dotted line). Blue triangles denote cool-core clusters and red diamonds non-cool core clusters. Filled symbols are the new strong lensing models, and open symbols are taken from the extended sample.

also Richard et al. 2009). We kept the centre of the ellipses fixed at the peak of the mass map and let the ellipticity  $e(a)$  and position angle  $\phi_{2D}(a)$  vary as free parameters with the semi major axis  $a$ . The resulting ellipticities are listed

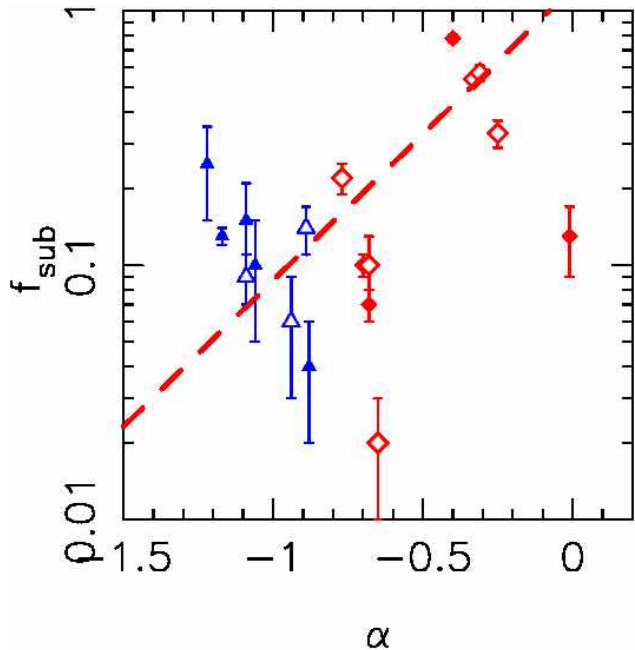


**Figure 11.** Relationship between substructure fraction,  $f_{\text{sub}}$ , and  $\alpha$  the slope of the gas density profile at  $0.04, r_{500}$ , as a measure of the strength of cooling in the cluster cores. Symbols are identical to Fig. 8. The dashed line shows the best-fit relation to the data.

in Table 7, and the distribution is plotted in Fig. 13. We also show in this figure the predicted distributions from Oguri & Blandford (2008), both for the underlying mass-selected cluster population, and for clusters with the largest Einstein radii. Oguri & Blandford interpreted the difference between these two distributions, with the latter peaking at smaller ellipticities than the former, as implying that the major axis the 3D mass distributions of strong-lensing clusters are more likely to be closely aligned with our line of sight through the clusters. Strong-lensing clusters are therefore expected to be rounder on the sky than non-strong-lensing clusters.

Our observed distribution agrees better with the predicted distribution of large Einstein radii clusters than with the mass-selected population, however we detect a peak at  $e_{2D} \simeq 0.65$ . This peak contains A 521 and A 1201, the two clusters in our sample with the smallest Einstein radii, demonstrating that clusters with small Einstein radii can still be strong lensing clusters if background galaxies are fortuitously aligned. We therefore exclude these two clusters from the observed distribution and fit a normal distribution to the other 18 clusters, obtaining:  $\langle e_{2D} \rangle = 0.34 \pm 0.14$

## 5 SUMMARY AND DISCUSSION

We have presented a strong lensing analysis of 20 massive galaxy clusters from the X-ray selected LoCuSS sample, all of which contain at least one spectroscopically-confirmed multiply-imaged background galaxy. Ten of the sample are new strong-lensing clusters for which we present the first detailed parametric lens models based on new spectroscopic redshift measurements at the Keck I telescope. All of the

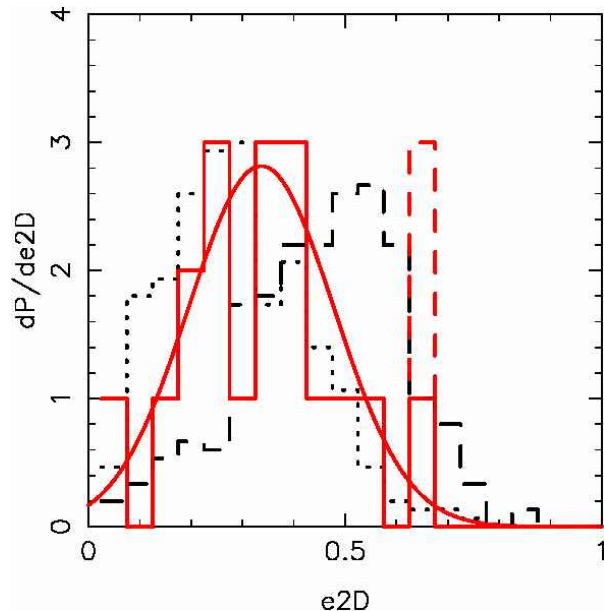


**Figure 13.** Observed distribution of 2d ellipticities (red solid histogram) compared with predictions from simulations by Oguri & Blandford (2008), for an unbiased cluster population (black dashed histogram) and a cluster population producing the largest Einstein radii (black dotted histogram). The observed peak at  $e_{2D} \simeq 0.65$  is dominated by A 1201 and A 521, the 2 clusters with the smallest Einstein radii (red dot-dashed histogram). The red solid curve shows the gaussian fit to the probability distribution.

clusters are well described by a parametric mass distribution containing one or several cluster-scale dark-matter halos centred on the brightest peaks of the cluster K-band light. We used our parametric models to compute maps of the mass distribution in the cluster cores, and thus to measure the projected mass and fraction of that mass associated with substructures within  $R \leq 250\text{kpc}$ . We have compared these measurements with observations of the baryons within the clusters, employing X-ray and K-band data to probe the intracluster medium and evolved stars respectively. Our main results are summarized below:

(i) The Einstein radius for a typical source redshift of  $z = 2$  spans  $4'' \leq \theta_E(z = 2) \leq 47''$  and is lognormally distributed, peaking at  $\langle \log_{10} \theta_E \rangle = 1.16 \pm 0.28$ , where the uncertainty is width of the distribution. Famous clusters with a large Einstein Radius, A 1689 and A 1703, are thus “outliers” at  $2\sigma$  and  $1.5\sigma$  above the mean respectively. We also compare the observed distribution with that predicted from the Millennium Simulation, and find that the peak of the predicted distribution lies at  $\sim 5''$ , i.e.  $\sim 1.7\sigma$  below that of the observed distribution.

(ii)  $\theta_E(z = 2)$  is correlated with  $M_{SL}(R < 250\text{kpc})$ , the projected mass of the cluster core obtained from the strong lens models. We find that “disturbed” clusters, i.e. those with an offset between the centroid of their X-ray emission and the optical centroid of their BCG of  $> 0.01r_{500}$ , typically lie below the best-fit  $\theta_E - M_{SL}$  relation. We interpret this as arising from a combination of (i) cluster-cluster mergers (assumed to be responsible for the X-ray/BCG offset) acting to soften the cluster density profile, and thus reduce  $\theta_E$ , and (ii) an orientation effect, i.e. that the major axis of disturbed

clusters tends to be closer to orthogonal to the line of sight through the cluster, whilst undisturbed clusters tend to have their major axis parallel with the line of sight.

(iii) The ratio of strong-lensing- and X-ray-based projected cluster mass measurements within  $R < 250\text{kpc}$  is measured to be  $M_{SL}/M_X = 1.3$ , discrepant with unity at  $3\sigma$ . This X-ray/lensing mass discrepancy depends on the structure of the cluster core – we detect a positive correlation between  $M_{SL}/M_X$  and the fraction of cluster mass associated with substructures within  $R < 250\text{kpc}$ ,  $f_{\text{sub}}$ , at  $2\sigma$  significance. We interpret this as evidence that the cluster-cluster merger activity associated with cluster substructure is responsible for departures from hydrostatic equilibrium.

(iv) The substructure fraction,  $f_{\text{sub}}$ , is also correlated with  $\alpha$ , the slope of the logarithmic gas density profile at  $0.04r_{500}$ , in the sense that clusters with steeper (more negative  $\alpha$ ) gas density profiles have smaller values of  $f_{\text{sub}}$ , and vice versa. The gas density profile slope is used as an indicator of the strength of cooling in the intracluster medium, the steepest slopes ( $\alpha \lesssim 0.85$ ) being identified as “cool core clusters”. This direct empirical relationship between  $\alpha$  and  $f_{\text{sub}}$ , implies a connection between the cluster-cluster mergers and the strength of cooling in cluster cores.

(v) We also find a strong correlation between  $f_{\text{sub}}$  and the dominance of the BCG in the sense that clusters with more substructure have less dominant BCGs. This suggests that measures of BCG dominance, including the luminosity gap statistic (difference between the magnitudes of the first and second ranked galaxies), may be a useful probe of cluster substructure.

(vi) The distribution of cluster core ellipticities, measured from the mass maps that are in turn computed from the parametric lens models, are consistent with the predicted ellipticity distribution of strong-lensing clusters.

This is the largest published sample of strong-lensing clusters to date – a  $4\times$  increase in sample size from Smith et al. (2005). Overall our empirical results are consistent with those of Smith et al. in that a straightforward interpretation is that cluster-cluster mergers play a prominent role in shaping the observed properties of cluster cores. This is most striking in the X-ray/lensing comparisons, i.e. significant detection of a 30% X-ray/lensing mass discrepancy, and a dependence of this discrepancy on structure of the cluster core. This is underlined by the correlation between  $f_{\text{sub}}$  and  $\alpha$  – implying that cluster-cluster mergers both cause departures from hydrostatic equilibrium and play a role in moderating the cooling of gas in cluster cores. This latter point remains controversial (e.g. Poole et al. 2008; Burns et al. 2008), and we caution that the distribution of formation epochs, and other physical processes such as pre-heating may ultimately modify our simplistic interpretation.

We also note that the clusters with the largest Einstein radii in our sample (A 1689 and A 1703) are  $\lesssim 2\sigma$  above the mean of the best-fit log-normal distribution, implying that  $\sim 2 - 7\%$  of larger samples will contain comparable clusters. We also speculate that the  $\sim 1.7\sigma$  discrepancy between the peak of the observed and predicted Einstein radius distributions may be in part attributable to the presence of baryons in the observed universe, in contrast to the dark matter only simulations on which the prediction is based. Certainly, the discrepancy is likely over-estimated because of the current

computational limitations on numerical simulations, namely that even the most advanced simulations such as the Millennium simulation do not embrace sufficient volume at sufficient numerical resolution to contain a representative sample of the most massive strong-lensing clusters. In summary, we find no compelling evidence from our statistical analysis of a sample of strong lensing clusters to support recent claims that clusters with large Einstein radii present a challenge to the CDM paradigm (Broadhurst & Barkana 2008).

This article has concentrated on clusters observable from Mauna Kea with the Keck-I telescope. In the future we will expand this sample to include Southern clusters that we have also observed with *HST* and followed up spectroscopically with VLT and Gemini-S (P. May et al., in preparation). Similar studies of clusters at  $z > 0.3$  from the MASSive Cluster Survey (Ebeling et al. 2001, 2007) will allow evolution in the properties of cluster cores to be probed (e.g. Smith et al. 2009a, Richard et al. in preparation). Within LoCuSS, future work will include combining these strong lens models with our recently published weak-lensing analysis of Subaru observations (Okabe et al. 2009) – this will allow a detailed investigation of the structure of the cluster mass distributions across a wide range of physical scales. The well-constrained lens models presented here are also well-suited to be utilized in gravitational telescope searches for very high redshift galaxies (Maizy et al. 2009), following, for example, Kneib et al. (2004); Richard et al. (2006, 2008); Bouwens et al. (2009). Finally, we have presented optical spectra of lensed background galaxies at  $z \sim 1 - 4$ , which are magnified by 1 – 4 magnitudes from strong lensing. These sources are well suited for further high resolution spectroscopic follow-up, such as near-infrared IFU observations (Swinbank et al. 2009).

## ACKNOWLEDGMENTS

We thank our colleagues in the LoCuSS collaborations for much support, encouragement and help. We acknowledge useful discussions with Andrew Newman, Masmune Oguri, Arif Babul, Giovanni Covone, Timothy James, Alastair Edge and Ian Smail. We are grateful for Matt Lehnert, Christian Tapken and Nicole Nesvadba for their spectroscopic measurement of one of the systems. Mark Sullivan kindly observed long-slit data on A 611 for us. JR acknowledges support from an EU Marie-Curie fellowship. GPS acknowledges support from the Royal Society and STFC. JPK acknowledges support from the CNRS, from the Agence Nationale de la Recherche grant ANR-06-BLAN-0067, and from the French-Israelian collaboration project 07-AST-F9. AJRS acknowledges support from STFC. ML acknowledges the Centre National d’ Etudes Spatiales (CNES) for their support. The Dark Cosmology Centre is funded by the Danish National Research Foundation. Results are partially based on observations made with the NASA/ESA Hubble Space Telescope and the Keck telescope. The authors recognize and acknowledge the very significant cultural role and reverence that the summit of Mauna Kea has always had within the indigenous Hawaiian community. We are most fortunate to have the opportunity to conduct observations from this mountain.

## REFERENCES

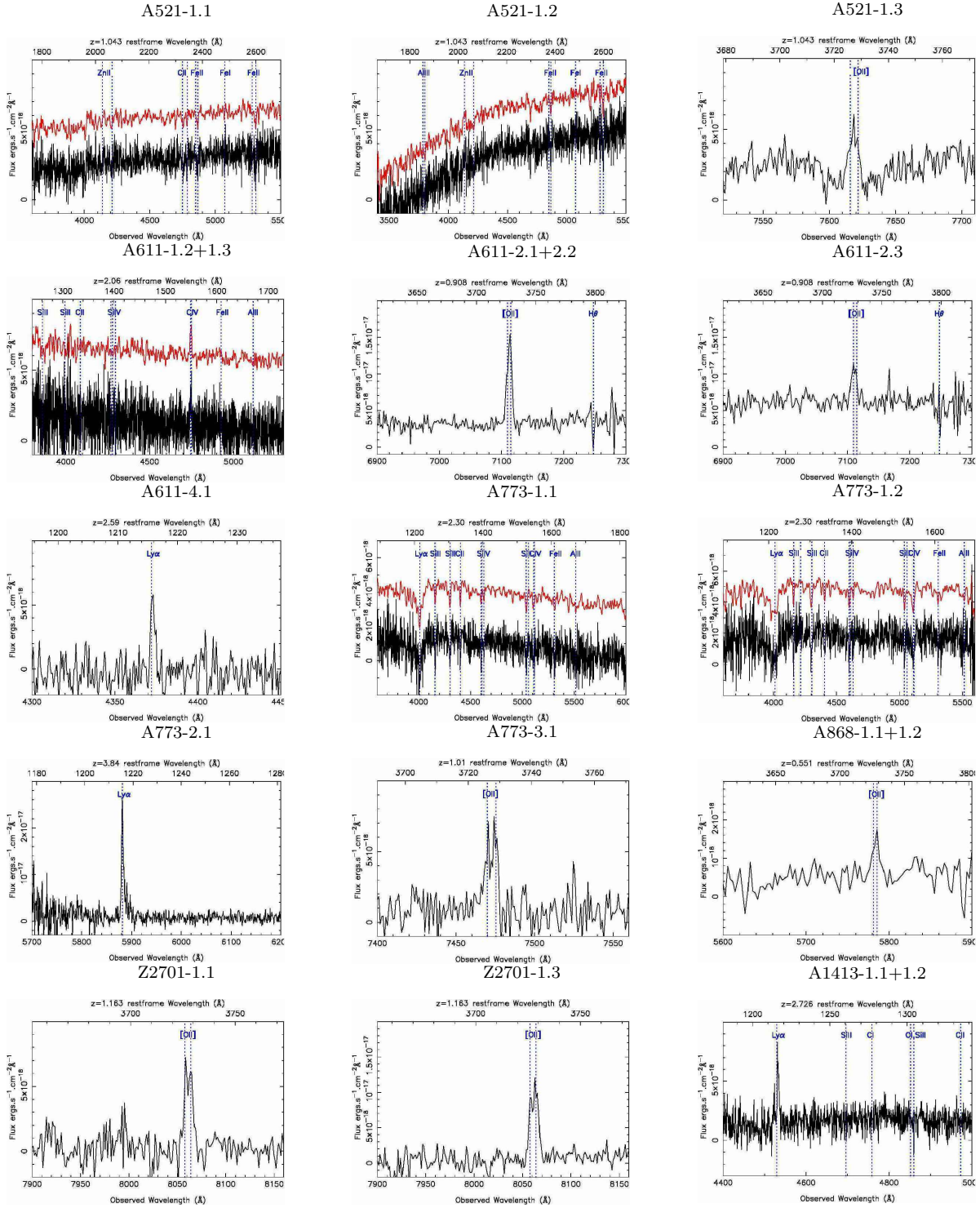
- Albrecht A., Bernstein G., Cahn R., Freedman W. L., Hewitt J., Hu W., Huth J., Kamionkowski M., Kolb E. W., Knox L., Mather J. C., Staggs S., Suntzeff N. B., 2006, arXiv:astro-ph/0609591
- Allen S. W., 1998, MNRAS, 296, 392
- Ascasibar Y., Diego J. M., 2008, MNRAS, 383, 369
- Bardeau S., Soucail G., Kneib J.-P., Czoske O., Ebeling H., Hudelot P., Smail I., Smith G. P., 2007, A&A, 470, 449
- Bernardi M., Sheth R. K., Annis J., Burles S., Eisenstein D. J., Finkbeiner D. P., Hogg D. W., Lupton R. H., Schlegel D. J., SubbaRao M., Bahcall N. A., Blakeslee J. P., Brinkmann J., Castander F. J., Connolly, 2003, AJ, 125, 1849
- Bertin E., Arnouts S., 1996, A&AS, 117, 393
- Blindert K., Yee H. K. C., Gladders M. D., Ellingson E., 2004, in IAU Colloq. 195: Outskirts of Galaxy Clusters: Intense Life in the Suburbs, Diaferio A., ed., pp. 215–219
- Böhringer H., Schuecker P., Guzzo L., Collins C. A., Voges W., Cruddace R. G., Ortiz-Gil A., Chincarini G., De Grandi S., Edge A. C., MacGillivray H. T., Neumann D. M., Schindler S., Shaver P., 2004, A&A, 425, 367
- Bonamente M., Joy M., LaRoque S. J., Carlstrom J. E., Nagai D., Marrone D. P., 2008, ApJ, 675, 106
- Bouwens R. J., Illingworth G. D., Bradley L. D., Ford H., Franx M., Zheng W., Broadhurst T., Coe D., Jee M. J., 2009, ApJ, 690, 1764
- Brainerd T. G., Specian M. A., 2003, ApJ, 593, L7
- Broadhurst T., Benítez N., Coe D., Sharon K., Zekser K., White R., Ford H., Bouwens R., Blakeslee J., Clampin M., Cross N., Franx M., Frye B., Hartig G., Illingworth G., Infante L., Menanteau F., Meurer G., Postman M., Ardila D. R., Bartko F., Brown R. A., Burrows C. J., Cheng E. S., Feldman P. D., Golimowski D. A., Goto T., Gronwall C., Herranz D., Holden B., Homeier N., Krist J. E., Lesser M. P., Martel A. R., Miley G. K., Rosati P., Sirianni M., Sparks W. B., Steindling S., Tran H. D., Tsvetanov Z. I., Zheng W., 2005, ApJ, 621, 53
- Broadhurst T. J., Barkana R., 2008, MNRAS, 390, 1647
- Bruzual G., Charlot S., 2003, MNRAS, 344, 1000
- Burns J. O., Hallman E. J., Gantner B., Motl P. M., Norman M. L., 2008, ApJ, 675, 1125
- Carlstrom J. E., Holder G. P., Reese E. D., 2002, ARA&A, 40, 643
- Coleman G. D., Wu C.-C., Weedman D. W., 1980, ApJS, 43, 393
- Covone G., Kneib J.-P., Soucail G., Richard J., Jullo E., Ebeling H., 2006, A&A, 456, 409
- Ebeling H., Barrett E., Donovan D., Ma C.-J., Edge A. C., van Speybroeck L., 2007, ApJ, 661, L33
- Ebeling H., Edge A. C., Allen S. W., Crawford C. S., Fabian A. C., Huchra J. P., 2000, MNRAS, 318, 333
- Ebeling H., Edge A. C., Böhringer H., Allen S. W., Crawford C. S., Fabian A. C., Voges W., Huchra J. P., 1998, MNRAS, 301, 881
- Ebeling H., Edge A. C., Henry J. P., 2001, ApJ, 553, 668
- Edge A. C., Smith G. P., Sand D. J., Treu T., Ebeling H., Allen S. W., van Dokkum P. G., 2003, ApJ, 599, L69
- Elíasdóttir Á., Limousin M., Richard J., Hjorth J., Kneib J.-P., Natarajan P., Pedersen K., Jullo E., Paraficz D., 2007, astro-ph/0710.5636
- Ellis R., Allington-Smith J., Smail I., 1991, MNRAS, 249, 184
- Faber S. M., Jackson R. E., 1976, ApJ, 204, 668
- Gehrels N., 1986, ApJ, 303, 336
- Golse G., Kneib J.-P., 2002, A&A, 390, 821
- Haines C. P., Smith G. P., Egami E., Ellis R. S., Moran S. M., Sanderson A. J. R., Merluzzi P., Busarello G., Smith R. J., 2009a, ApJ, 704, 126
- Haines C. P., Smith G. P., Egami E., Okabe N., Takada M., Ellis R. S., Moran S. M., Umetsu K., 2009b, MNRAS, 396, 1297
- Halkola A., Seitz S., Pannella M., 2007, ApJ, 656, 739
- Hernquist L., 1990, ApJ, 356, 359
- Hjorth J., Oukbir J., van Kampen E., 1998, MNRAS, 298, L1
- Jullo E., Kneib J.-P., 2009, MNRAS, 395, 1319
- Jullo E., Kneib J.-P., Limousin M., Elíasdóttir Á., Marshall P. J., Verdugo T., 2007, New Journal of Physics, 9, 447
- Kelson D. D., 2003, PASP, 115, 688
- Kneib J., Hudelot P., Ellis R. S., Treu T., Smith G. P., Marshall P., Czoske O., Smail I., Natarajan P., 2003, ApJ, 598, 804
- Kneib J.-P., 1993, Ph.D. Thesis
- Kneib J.-P., Ellis R. S., Santos M. R., Richard J., 2004, ApJ, 607, 697
- Kneib J.-P., Ellis R. S., Smail I., Couch W. J., Sharples R. M., 1996, ApJ, 471, 643
- Kurk J., Cimatti A., Zamorani G., Halliday C., Mignoli M., Pozzetti L., Daddi E., Rosati P., Dickinson M., Bolzonella M., Cassata P., Renzini A., Franceschini A., Rodighiero G., Berta S., 2009, arXiv:astro-ph/0906.4489
- Limousin M., Kneib J. P., Bardeau S., Natarajan P., Czoske O., Smail I., Ebeling H., Smith G. P., 2007a, A&A, 461, 881
- Limousin M., Richard J., Jullo E., Kneib J.-P., Fort B., Soucail G., Elíasdóttir Á., Natarajan P., Ellis R. S., Smail I., Czoske O., Smith G. P., Hudelot P., Bardeau S., Ebeling H., Egami E., Knudsen K. K., 2007b, ApJ, 668, 643
- Limousin M., Richard J., Kneib J.-P., Brink H., Pelló R., Jullo E., Tu H., Sommer-Larsen J., Egami E., Michałowski M. J., Cabanac R., Stark D. P., 2008, A&A, 489, 23
- Lin Y.-T., Mohr J. J., Gonzalez A. H., Stanford S. A., 2006, ApJ, 650, L99
- Maizy A., Richard J., De Leo M. A., Pello R., Kneib J. P., 2009, arXiv:astro-ph/0910.4910
- Marrone D. P., Smith G. P., Richard J., Joy M., Bonamente M., Hasler N., Hamilton-Morris V., Kneib J., Culverhouse T., Carlstrom J. E., Greer C., Hawkins D., Hennessy R., Lamb J. W., Leitch E. M., Loh M., Miller A., Mroczkowski T., Muchovej S., Pryke C., Sharp M. K., Woody D., 2009, ApJ, 701, L114
- Maurogordato S., Le Fèvre O., Proust D., Vanderriest C., Cappi A., 1996, Bulletin d'information du telescope Canada-France-Hawaii, 34, 5
- Maurogordato S., Proust D., Beers T. C., Arnaud M., Pelló R., Cappi A., Slezak E., Kriessler J. R., 2000, A&A, 355, 848
- Miralda-Escude J., Babul A., 1995, ApJ, 449, 18
- Nagai D., 2006, ApJ, 650, 538
- Nagai D., Vikhlinin A., Kravtsov A. V., 2007, ApJ, 655, 98
- Natarajan P., Kneib J., Smail I., 2002, ApJ, 580, L11
- Natarajan P., Kneib J.-P., Smail I., Treu T., Ellis R., Moran

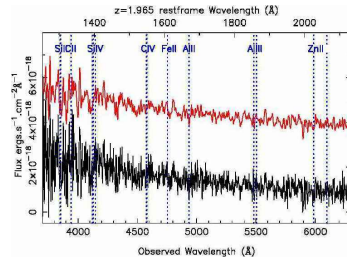
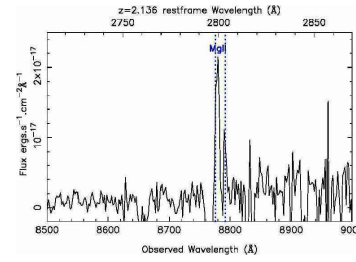
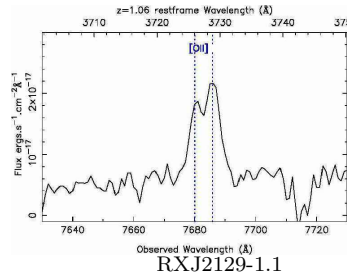
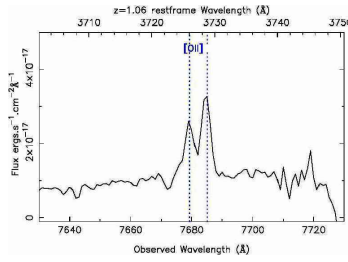
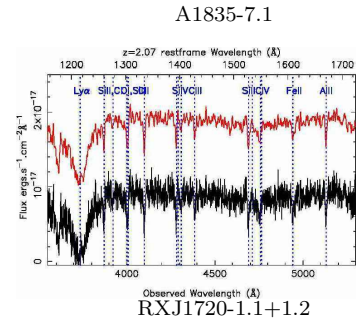
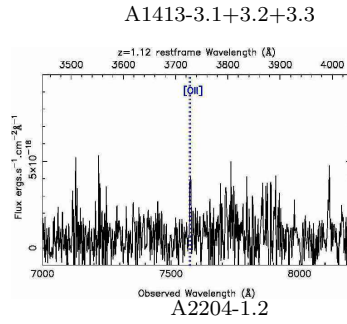
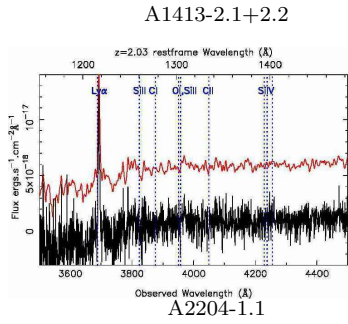
- S., Limousin M., Czoske O., 2009, *ApJ*, 693, 970
- Navarro J. F., Frenk C. S., White S. D. M., 1997, *ApJ*, 490, 493
- Oguri M., Blandford R. D., 2008, *MNRAS* accepted, astro-ph/0808.0192
- Okabe N., Takada M., Umetsu K., Futamase T., Smith G. P., 2009, arXiv:astro-ph/0903.1103
- Oke J. B., Cohen J. G., Carr M., Cromer J., Dingizian A., Harris F. H., Labrecque S., Lucinio R., Schaal W., Epps H., Miller J., 1995, *PASP*, 107, 375
- Poole G. B., Babul A., McCarthy I. G., Sanderson A. J. R., Fardal M. A., 2008, *MNRAS*, 391, 1163
- Rasia E., Ettori S., Moscardini L., Mazzotta P., Borgani S., Dolag K., Tormen G., Cheng L. M., Diaferio A., 2006, *MNRAS*, 369, 2013
- Richard J., Kneib J.-P., Jullo E., Covone G., Limousin M., Ellis R., Stark D., Bundy K., Czoske O., Ebeling H., Soucaïl G., 2007, *ApJ*, 662, 781
- Richard J., Pei L., Limousin M., Jullo E., Kneib J. P., 2009, *A&A*, 498, 37
- Richard J., Pelló R., Schaerer D., Le Borgne J.-F., Kneib J.-P., 2006, *A&A*, 456, 861
- Richard J., Stark D. P., Ellis R. S., George M. R., Egami E., Kneib J.-P., Smith G. P., 2008, *ApJ*, 685, 705
- Rosati P., Stanford S. A., Eisenhardt P. R., Elston R., Spinrad H., Stern D., Dey A., 1999, *AJ*, 118, 76
- Sand D. J., Treu T., Ellis R. S., Smith G. P., 2005, *ApJ*, 627, 32
- Sand D. J., Treu T., Smith G. P., Ellis R. S., 2004, *ApJ*, 604, 88
- Sanderson A. J. R., Edge A. C., Smith G. P., 2009a, astro-ph/0906.1808
- Sanderson A. J. R., O'Sullivan E., Ponman T. J., 2009b, *MNRAS*, 395, 764
- Sanderson A. J. R., Ponman T. J., 2009, arXiv:astro-ph/0910.3212
- Schmidt R. W., Allen S. W., Fabian A. C., 2001, *MNRAS*, 327, 1057
- Schuecker P., Böhringer H., Collins C. A., Guzzo L., 2003, *A&A*, 398, 867
- Seidel G., Bartelmann M., 2007, *A&A*, 472, 341
- Smail I., Ellis R. S., Dressler A., Couch W. J., Oemler A. J., Sharples R. M., Butcher H., 1997, *ApJ*, 479, 70
- Smail I., Smith G. P., Ivison R. J., 2005, *ApJ*, 631, 121
- Smith G. P., Ebeling H., Limousin M., et al., 2009a, *ApJ*, 707, 163
- Smith G. P., Edge A. C., Eke V. R., Nichol R. C., Smail I., Kneib J., 2003, *ApJ*, 590, L79
- Smith G. P., Khosroshahi H. G., et al., 2009b, *MNRAS*, submitted
- Smith G. P., Kneib J., Ebeling H., Czoske O., Smail I., 2001, *ApJ*, 552, 493
- Smith G. P., Kneib J.-P., Smail I., Mazzotta P., Ebeling H., Czoske O., 2005, *MNRAS*, 359, 417
- Smith G. P., Smail I., Kneib J.-P., Davis C. J., Takamiya M., Ebeling H., Czoske O., 2002, *MNRAS*, 333, L16
- Smith G. P., Taylor J. E., 2008, *ApJ*, 682, L73
- Stott J. P., Pimblet K. A., Edge A. C., Smith G. P., Wardlow J. L., 2009, *MNRAS*, 394, 2098
- Swinbank M., Webb T., Richard J., Bower R., Ellis R., Illingworth G., Jones T., Kriek M., Smail I., Stark D., Van Dokkum P., 2009, *MNRAS*, 400, 1121
- Taylor J. E., Babul A., 2005, *MNRAS*, 364, 535
- Tyson J. A., Kochanski G. P., dell'Antonio I. P., 1998, *ApJ*, 498, L107+
- Vikhlinin A., Burenin R., Forman W. R., Jones C., Hornstrup A., Murray S. S., Quintana H., 2007, in *Heating versus Cooling in Galaxies and Clusters of Galaxies*, Böhringer H., Pratt G. W., Finoguenov A., Schuecker P., eds., pp. 48–+
- Vikhlinin A., Kravtsov A., Forman W., Jones C., Markevitch M., Murray S. S., Van Speybroeck L., 2006, *ApJ*, 640, 691
- Visvanathan N., Sandage A., 1977, *ApJ*, 216, 214
- Wilman R. J., Edge A. C., Swinbank A. M., 2006, *MNRAS*, 371, 93
- Zhang Y.-Y., Finoguenov A., Böhringer H., Kneib J.-P., Smith G. P., Kneissl R., Okabe N., Dahle H., 2008, *A&A*, 482, 451

## APPENDIX A: SPECTRA OF MULTIPLE IMAGES



Figure A1. Extracted spectra of multiple images from the current sample. We mark the prominent spectral features used to derive the redshift.





**APPENDIX B: BEST FIT PARAMETERS OF  
OTHER MASS MODELS**

**Table B1.** Best-fit parameters of the mass models. For each mass component, we give the centre, ellipticity, orientation, core and cut radii, as well as central velocity dispersion of the dPIE profile. The following column gives the image plane RMS of this model

Cluster	Comp.	$\Delta\alpha$ [ $''$ ]	$\Delta\delta$ [ $''$ ]	$e$	$\theta$ [deg]	$r_{\text{core}}$ [kpc]	$r_{\text{cut}}$ [kpc]	$\sigma_0$ [km s $^{-1}$ ]	rms [ $''$ ]
A383	DM1	[-0.3]	[0.5]	0.15±0.05	123.7±2.4	285.0±38.9	[1000.0]	1976±132	0.22
	BCG	[0.1]	[-0.1]	[0.189]	[96.400]	[0.0]	[40.0]	117±40	
	PERT1	[14.9]	[-16.7]	[0.125]	[-6.900]	9.5±2.8	15.3±8.7	412±110	
	L* gal					[0.15]	18.7±10.1	141±29	
A963	DM1	[0.0]	[0.0]	[0.209]	[85]	23.2±2.8	[1000.0]	743±173	0.22
	BCG	[0.0]	[0.0]	[0.209]	[85.0]	[0.0]	47.2±4.2	210±27	
	L* gal					[0.15]	[45]	[158]	
A1201	DM1	[0.0]	[0.0]	0.99±0.26	57.2±7.6	[75.0]	[1000.0]	1085±205	0.07
	BCG	[0.0]	[0.0]	[0.705]	[59.8]	[0.0]	20.2±55.3	250±44	
	L* gal					[0.15]	[45]	[158]	
A2218	DM1	3.1±0.5	20.8±0.2	0.04±0.02	38.0±0.6	58.3±1.0	596.2±4.4	697±1	0.12
	DM2	-16.9±0.1	-21.7±0.6	0.32±0.01	9.2±0.5	119.7±2.7	484.1±189.4	992±7	
	BCG	[-0.5]	[0.1]	[0.46]	[52.4]	5.2±2.6	38.1±2.81	506±2	
	PERT1	[-16.0]	[-10.3]	[0.180]	[80.4]	1.1±0.3	1.3±0.3	425±3	
	PERT2	[-46.1]	[-49.1]	[0.199]	[59.4]	1.5±2.2	28.6±0.5	277±1	
	L* gal					[0.15]	[45]	[158]	
A2219	DM1	[0.1]	[0.2]	0.65±0.03	32.9±0.4	[77.0]	[1000.0]	854±19	1.13
	DM2	[-39.2]	[-32.0]	[0.1]	[7.6]	[157]	[1000.0]	781±28	
	DM3	[-22.9]	[4.5]	[0.0]	[0.0]	7.9±1.2	[1000.0]	328±13	
	BCG	[0.0]	[0.0]	[0.442]	[29.0]	[0.041]	12.2±23.1	714±111	
	L* gal					[0.15]	2.1±15.6	264±93	
A2390	DM1	38.9±8.2	27.4±0.7	0.61±0.08	215.1±0.7	592.3±15.7	[2000.0]	2038±54	0.13
	BCG	[-0.9]	[-1.4]	0.03±0.06	30.5±5.5	29.9±0.5	294.8±24.5	633±2	
	PERT1	[46.9]	[12.8]	0.35±0.09	143.7±4.3	[0.05]	41.5±2.8	152±1	
	L* gal					[0.15]	[45]	[158]	
A2667	DM1	0.1±0.9	-0.5±0.8	0.32±0.05	-44.1±0.5	82.5±5.3	[1298.629]	1114±26	0.28
	L* gal					[0.15]	[45]	109±13	